Norwegian University
of Life Sciences

Master's Thesis 2017 30 ECTS
Department of Science and Technology

Electrical characterization of silicon nitride and silicon oxynitride thin films for solar cell applications

Heidi Tønnesson
Master of Science Education

Preface

Knowing that I am about to finish my studies at NMBU is a bizarre feeling, and I am not sure how I feel about it yet. Still, I am truly happy that I got the opportunity to finish my master's degree by doing research within my favorite field: Solar energy. My time at the solar department at IFE has been great; I absolutely do not feel ready to leave you yet. You have all been so welcoming, helpful, funny and smart. And there is a lot of people I want to thank.

First and foremost, thank you, Erik, for being an awesome supervisor. Your knowledge, combined with your enthusiasm, has been a great inspiration. You deserve an applauding otter.

Thank you, Halvard, for your patience, guidance and for all your help. And for writing great papers, which have filled both my head and my bibliography with smart stuff.

Thank you, Therese, for the coffee breaks, for taking me under your wing and teaching me how all the lab equipment works. And for being honest and telling me everything you didn't know - it made me feel much better!

Thank you, Arne, for your optimism, valuable advice and for convincing me that I needed a Christmas break.

A big thanks to all of you I have been so lucky to share study quarters with. And thank you, Marte, for providing me with cake this last weekend of intense writing. It made everything so much better.

I would also like to thank my parents and Salto. I am grateful for having a dog that does not eat my homework.

And finally, thank you to my Erik, who have spiced up my thesis with un-passivated dachshunds playing in the sun. And for cooking, cleaning and listening to endless talk about samples and simulations that didn't work. You are my sunshine!

Kjeller, January 29th 2017.

Heidi Tønnesson

Sammendrag

På grunn av rekombinasjon er overflaten av silisiumkrystaller en stor bidragsyter til effektivitetstap i solceller, og overflatepassivisering har derfor en stor betydning i produksjonen av høyeffektive solceller. I denne studien blir overflatepassiviseringsegenskapene til silisiumnitrid- og silisiumoksynitrid-tynnfilmer studert ved å modulere den faste ladningstettheten i materialene. Hensikten er å øke forståelsen for muligheten for økning i ladningsbærertettheten i silisiumnitrid-filmer for dermed å øke felteffektpassiviseringen. Egenskapene som studeres er tykkelse, sammensetning, kjemisk passivisering og felteffektpassivisering. Videre er passiveringsegenskapene for enkeltfilmer av silisiumnitrid (forkortet nitrider) og stablene av silisiumoksinitrid toppet med silisiumnitrid sammenliknet og karakteriseringsmetodenes egnethet er vurdert

Prøvesettet bestod av fire nitridfilmer og to stabler. SiN_x-filmene ble deponert med to ulike sammensetninger - 10 sccm og 5 sccm SiH_4 - med to forskjellige tykkelser; 80 nm og 100 nm. Stablene ble deponert med lik tykkelse og sammensetning av mellomlaget SiO_xN_y, men med to forskjellige sammensetninger av SiN_x-topplaget: 20 sccm og 10 sccm SiH_4.

Levetidsmålinger ble gjennomført uten oppladning. Den effektive levetiden, τ_{eff}, for nitridene var i området 100 µs, mens stablene var i området 1500 µs. Alle silisiumrike prøver ga høyere τ_{eff} sammenlignet med de nitridrike prøvene. Dette er et resultat av bedre kjemisk passivering for de silisiumrike filmene. Dette mønsteret ble også observert i målinger gjort med fotoluminescensavbildning med påsatt spenning (PL–V). Kapasitans–spennings-målinger ble utført med og uten oppladning til –30 V. Resultatene ble brukt til å beregne tettheten av de faste ladningene, Q_f. Resultatene viste at nitridene var oppladbare, den øvre grensen for Q_f ble imidlertid ikke nådd på grunn av instrumentelle begrensninger. Stablene viste seg å være ladbare i mindre grad sammenliknet med nitridene. Tykkelsen viste seg å være den mest innflytelsesrike variabelen blant nitridfilmene, mens sammensetningen var den viktigste parameteren for stablene. Med utgangspunkt i litteraturen har Karakteriseringsmetodene som er blitt vist forventede resultater for nitridfilmene. De elektriske karakteriseringsmetodene, C-V og PL-V, gav mer komplekse resultater for stablene. Generelt har stablene har vist høyere grad av passivering, men de er mindre oppladbare sammenliknet med nitridene.

Abstract

The surface of the silicon crystal is a large contributor to efficiency losses in solar cells due to recombination. As the wafer thickness decreases, surface passivation is of great importance to produce high performing solar cells. This work studies the surface passivating properties of silicon nitride (abbreviation: nitrides), and silicon oxynitrides capped with silicon nitride (abbreviation: stacks) thin films by modulating the fixed charge densities in the materials. The study is performed to increase the understanding of the possibility of increasing the charge carrier density in silicon nitride films for improved field effect passivation. The properties for investigation are thickness, composition, chemical passivation and field effect passivation. Moreover, the passivation properties of stacks compared to the single layer nitrides are studied, and the suitability of the characterization methods is discussed.

The sample set consisted of four nitride films and two stacks. The SiN_x films are deposited with two different compositions and two different thicknesses: 10 sccm and 5 sccm silane flow, and 80 nm and 100 nm. The stacks are deposited with equal thickness and equal composition of the buffer layer SiO_xN_y, with two different compositions of the SiN_x capping layers; 20 sccm and 10 sccm silane flow.

All films showed good passivation properties prior to charging. The effective lifetime, τ_{eff}, of the nitrides were approximately 100 µs, while the stacks were exceeding 1500 µs. All silicon rich samples yield a higher τ_{eff} compared to the nitride rich samples, which is a result of better chemical passivation. This pattern was also observed by photoluminescence imaging under applied bias (PL–V) measurements. Capacitance – voltage sweeps were performed with and without pre-soaking bias up to –30 V. The results were used to calculate fixed charge density, Q_f. The results showed that the nitrides are chargeable. However, the upper limit for Q_f was not reached due to instrumental limitations. The stacks showed to be less chargeable compared to the nitrides. The thickness turned out to be the most influential parameter among the stacks with regards to charging, while the composition showed to be the most influential parameter for the stacks. Considering the literature, all characterization methods have attained as-expected results for the nitrides. For the stacks, the electrical characterization methods, C–V and PL–V, have provided more complex results. Overall, the stacks have shown a higher degree of passivation, but are less chargeable than the nitrides.

Table of content

List of symbols

Symbol	Description	Unit
α_0	Smallest eigenvalue solution to Eq. 2.18	cm^{-1}
β	$q\ /k_BT$	V^{-1}
ε_0	Permittivity of free space	F/cm
ε_i	Insulator dielectric constant	-
ε_{si}	Dielectric constant for silicon	-
μ_n	Mobility of electrons	cm^2/Vs
μ_p	Mobility of holes	cm^2/Vs
σ_n	Capture cross section for electrons	cm^2
σ_p	Capture cross section for holes	cm^2
τ	Minority carrier lifetime	s
τ_b	Minority carrier lifetime in bulk	s
$\tau_{eff,min}$	Minimum effective lifetime	s
τ_{eff}	Effective lifetime	s
τ_{n0}	Capture time constant for electrons	s
τ_{p0}	Capture time constant for holes	s
τ_s	Surface lifetime	s
k_B	Boltzmann constant	eV/K
v_{th}	Thermal velocity for electrons	m/s
ϕ_n	Quasi-Fermi level for electrons	V
ϕ_p	Quasi-Fermi level for holes	V
ϕ_{PH}	Photon flux	$cm^{-2}s^{-1}$
ϕ_{PL}	Photo intensity	s^{-1}
χ_{Si}	Electron affinity of silicon	eV
ψ_s	Surface potential	V
Ψ	Ellipsometric parameter	-
Δ	Ellipsometric parameter	-
$\Delta\sigma$	Excess photoconductance	S/cm
$\Delta\phi_{ms}$	Metal – semiconductor work function difference	V
Δn_s	Excess carrier concentration at the surface	cm^{-3}
Δn	Excess electron density	
A	Area	cm^2
B_{Rad}	Radiative recombination coefficient	cm^3s^{-1}
C	Capacitance	F
C_{cal}	Calibration constant for PL-I	cm^3s
C_{fb}	Flatband capacitance	F

C_i	Insulator capacitance	F
C_{it}	Interface states capacitance	F
C_n, C_p	Auger coefficients for electrons and holes	cm^6s^{-1}
C_{sc}	Space charge region capacitance	F
C_{TOT}	Total capacitance	F
D	Minority carrier diffusion coefficient	cm^2/s
d_f	Thickness of insulator region containing fixed charges	cm
d_i	Thickness of insulator layer	cm
D_{it}	Interface state density	$cm^{-2}eV^{-1}$
E_c	Conduction band energy level	eV
E_f	Fermi energy level	eV
E_g	Band gap	eV
E_i	Intrinsic energy level	eV
E_t	Defect energy level	eV
E_v	Valence band energy level	eV
F_m	Metal work function	eV
G	Generation rate	$cm^{-3}s^{-1}$
I_{PL}	Detected photoluminescence intensity	counts/s
I_{ref}	Reference photocurrent	counts/s
J	Current	A
L_D	Debye length	cm
n	Electron concentration in the conduction band	cm^{-3}
n_0	Electron concentration at thermal equilibrium	cm^{-3}
n_1	Statistical parameter for SRH recombination, electrons	cm^{-3}
N_A	Acceptor doping concentration	cm^{-3}
n_b	Electron concentration in the bulk	cm^{-3}
N_D	Donor doping concentration	cm^{-3}
n_i	Intrinsic carrier concentration at thermal equilibrium	cm^{-3}
n_s	Surface electron concentration	cm^{-2}
N_t	Single defect level density	cm^{-3}
N_t	Concentration of single defect levels, surface states	cm^{-2}
OC	Optical constant for QSSPC	-
p	Hole concentration in the valence band	cm^{-3}
p_0	Hole concentration at thermal equilibrium	cm^{-3}
p_1	Statistical parameter for SRH recombination, holes	cm^{-3}
p_b	Hole concentration in the bulk	cm^{-3}
p_i	Intrinsic carrier concentration at thermal equilibrium	cm^{-3}
p_s	Surface hole concentration	cm^{-2}

q	Elementary charge	C
Q_f	Fixed charge density in the insulating layer	cm^{-2}
Q_g	Charge density in the metal electrode	cm^{-2}
Q_{it}	Charge density in the interface states	cm^{-2}
Q_{sc}	Charge density in the space charge region	cm^{-2}
R_f	Refractive index at 808 nm	-
R_p	Reflectance for p-polarized light	-
R_s	Reflectance for s-polarized light	-
S	Surface recombination velocity	cm/s
S_b	Back surface recombination velocity	cm/s
S_f	Front surface recombination velocity	cm/s
S_{max}	Surface recombination velocity with infinite bulk lifetime	cm/s
$S_{min,n}$	Added SRV contribution for $\psi_s < 0$ in PL-V	cm/s
$S_{min,p}$	Added SRV contribution for $\psi_s > 0$ in PL-V	cm/s
S_{n0}	Effective surface recombination parameter for electrons	cm/s
S_{p0}	Effective surface recombination parameter for holes	cm/s
T	Temperature	K
t	Time	s
U	Recombination rate	$cm^{-3}s^{-1}$
U_{Aug}	Auger recombination rate	$cm^{-3}s^{-1}$
U_b	Bulk recombination rate	$cm^{-3}s^{-1}$
U_{rad}	Radiative recombination rate	$cm^{-3}s^{-1}$
U_s	Surface recombination rate per area	$cm^{-2}s^{-1}$
U_{SRH}	SRH recombination rate	$cm^{-3}s^{-1}$
V_{fb}	Flatband voltage	V
V_g	Gate voltage	V
V_g	Gate voltage	V
V_i	Insulator voltage	V
W	Wafer thickness	cm
W_{ref}	Reference wafer thickness	cm

List of abbreviations

Abbreviation	Description
c-Si	Crystalline silicon
C–V	Capacitance–voltage
MIS	Metal-insulator-semiconductor
PECVD	Plasma enhanced chemical vapor deposition
PL-I	Photo luminescence imaging
PL-V	Photoluminescence imaging under applied bias
PV	Photovoltaic
QSSPC	Quasi-steady state photoconductance
SRH	Shockley-Read-Hall
SRV	Surface recombination velocity
VASE	Variable angle spectroscopic ellipsometry

CHAPTER 1

INTRODUCTION

In light of the climate changes, there has been an increasing global focus on renewable energy's role in abating the negative impacts. The EU has given generous subsidies to increase adoption. Combined with reduced production costs for solar cells, this has made solar energy the fastest growing renewable electricity production technology, with a global increase in installed capacity of 50 GW in 2015 (REN 21 2016).

Since 2008, the costs of solar cells have sunk by 80% (IEA 2016), but the technology still has room to become more competitive. Two main constraints needs to be lifted for making solar cells more competitive on the market: Improved conversion efficiency and further reduction of the costs.

Currently, c-Si is the leading photovoltaic technology, with a market share over 90% (ITRPV 2016). More than 61% of the production costs is attributable to the silicon (ITRPV 2016). By producing thinner wafers, the need for silicon is reduced. Although this is cost mitigating in production, the reduced thickness increases the required surface passivation of the cells.

The surface of the silicon crystal is a large contributor to efficiency losses due to recombination. As the wafer thickness decreases, surface passivation is of great importance to produce high performing solar cells. To achieve great passivation, a low surface recombination velocity (SRV) is needed. Figure 1-1 shows how the efficiency drops with the increase in SRV. The illustration is based on simplifications regarding normal cell operations to outline the main features of the SRV (Haug 2017).

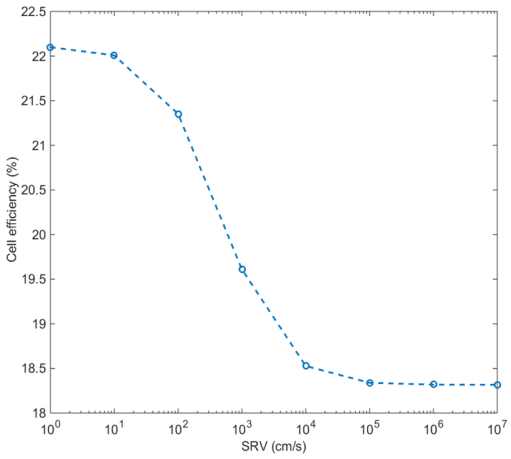

Figure 1-1: Cell efficiency as a function of SRV (Haug 2017).

The SRV depends on the concentration of carriers at the surface and the concentration of interface states. The interface states are caused by unsaturated atoms at the surface of the silicon substrate. The main strategy for reducing the unsaturated atoms is deposition of a thin film, typically with a large concentration of hydrogen. The hydrogen diffuses to the interface and binds with the unsaturated atoms. This method is called chemical passivation. Reduction of the carrier concentration is called field effect passivation, where a passivation layer containing fixed charges Q_f is deposited on the substrate. The fixed charges push either the holes or the electrons further down in the substrate, depending on the charges. Several passivation layers are currently studied to meet the technological needs. Silicon nitrides have previously showed potential with regards to passivation and the possibility of charging to increase the field effect passivation effect (Bazilchuck 2014).

1.1 Research questions

The object of this work is to increase the understanding of the possibility of using a newly developed method for increasing the charge carrier density in silicon nitride to improve surface passivation by field effect passivation. Six different passivation films will be considered and evaluated: Two silicon oxynitrides with capping layers of silicon nitride, and four silicon nitride films. The stacks are produced with an equal buffer layer of oxynitride, but with two different compositions of the nitride capping layer. The nitrides are divided in two different compositions deposited with two different thicknesses.

The research questions addressed in this thesis can be summarized as follows:

1) How are the stacks performing compared to the nitrides?
2) To what extent does the silicon/nitride ratio affect the passivation?
3) To what extent does the thickness of the films affect the passivation?
4) Is the thickness or the composition most influential on the passivation?
5) Are the characterization methods suitable?
6) What is the relative importance of the chemical and field effect passivation?

1.2 Thesis outline

The thesis is divided in six chapters:

Chapter 1 describes the motivation and the scope of the thesis. Chapter 2 provides the theory needed for the characterization and analysis. Chapter 3 presents the characterization methods. Chapter 4 describes the sample set. Chapter 5 presents the results with discussion. Chapter 6 concludes and summarizes the main findings.

CHAPTER 2

THEORY

This chapter outlines the physics of recombination in solar cells and requirements for surface passivation. The chapter is divided in five parts.

Section 2.1 presents the minority carrier lifetime and the physics behind the recombination processes, both in the bulk of the cell and at the surface. The three recombination processes; radiative recombination, Auger recombination and recombination via defects are presented. The latter one also called the Shockley-Read-Hall (SRH) recombination is also used for calculations of surface recombination.

Section 2.2 outlines the two surface passivation techniques: Chemical passivation and field effect passivation, where both techniques usually are combined to achieve good passivation.

Section 2.3 explains the behavior of the energy bands in a semiconductor both with, and without charges affecting the energy level at the surface. Further is the charge distribution explained using the Girisch model.

Section 2.4 presents the effective lifetime, which is the minority carrier life time of the bulk and the surface combined. The effective lifetime is usually the obtained results of lifetime measurements, such that distinction between them is needed.

Section 2.5 outlines different materials used for passivation of silicon and their properties.

2.1 Carrier recombination in crystalline silicon solar cells

Based on the work of Aberle (1999) and Haug (2014).

Recombination losses in a solar cell reduce its overall efficiency. To maximize the energy output, the generation of electron–hole-pairs must be maximized and the carrier recombination minimized. Recombination decreases both the open-circuit voltage and the short-circuit current of the solar cells. The recombination mechanisms for silicon solar cells will be further explained in this chapter.

Carrier recombination losses occur when generated electron–hole-pairs recombine before being spatially separated by the depletion layer. The probability of recombination increases the farther away from the depletion layer the generation happens. The minority charge carrier lifetime, τ, normally referred to as the lifetime, is the average time it takes for the minority charge carrier to recombine. The lifetime depends on the quality of the silicon, the doping level and the illumination level, and is defined as:

$$\tau \equiv \frac{\Delta n}{U} \tag{2.1}$$

where U is the net recombination rate and $\Delta n \equiv n - n_0$ is the injection level of the excess carrier. The injection level is the difference between the concentration of electrons in the conduction band n and the concentration of electrons at thermal equilibrium n_0.

There are three fundamental recombination processes with corresponding recombination rates and lifetimes: Radiative recombination, band-to-band Auger recombination and recombination via defects. Radiative and Auger-recombination is inherent to the material and may be seen as an upper limit for the recombination losses. Recombination via defects is caused by impurities or disruptions in the material and is a great contributor to efficiency losses at the surface and interface where the silicon is in contact with other materials.

2.1.1 Bulk recombination

In the volume of the solar cell, the silicon is isolated from the surroundings. The recombination mechanisms in the bulk are thus a result from the inherent properties of the silicon or the quality of the material. The three bulk mechanisms are further explained in this section.

Radiative recombination is the counter process of electron-hole-pair generation. An electron in the conduction band directly recombines with a hole in the valence band, releasing the excess energy as a photon with energy corresponding to the band gap. This process occurs more often in direct band gap semiconductors, such as GaAs, than in silicon which is an indirect band gap semiconductor. The generation rate of radiative recombination U_{rad} is calculated as:

$$U_{\mathrm{rad}} = B_{\mathrm{rad}}(np - n_i^2) \tag{2.2}$$

where B_{rad} is a material constant, n is the concentration of electrons in the conduction band, p is the concentration of holes in the valence band and n_i is the intrinsic carrier concentration at thermal equilibrium.

Band-to-band Auger recombination takes place when an electron in the conduction band recombines with a hole and transmits the excess energy to a third carrier. An electron is either pushed further up in the conduction band or a hole further down in the valence band. This process increases with the injection level and is the dominating recombination process in silicon solar cells. This implies that the carrier lifetime decreases with increasing injection level. The recombination rate related to the Auger recombination U_{Aug} is defined as:

$$U_{\mathrm{Aug}} = C_n n^2 p + C_p n p^2 \tag{2.3}$$

where C_n and C_p are Auger coefficients for electrons and holes respectively.

Recombination via defects is a process caused by impurities in the semiconductor crystal called traps, defect levels or recombination centers. These impurities create energy levels in the otherwise forbidden band gap. In this process, a defect level may attract both a hole from the valence band and an electron from the conduction band.

The Shockley-Read-Hall (SRH) theory describes the mechanisms behind recombination via defects. The recombination rate U_{SRH} is a result of a defect with concentration N_t and energy level E_t:

$$U_{\mathrm{SRH}} = \frac{v_{th} N_t (np - n_i^2)}{\frac{n + n_1}{\sigma_p} + \frac{p + p_1}{\sigma_n}} = \frac{np - n_i^2}{\tau_{p0}(n + n_1) + \tau_{n0}(p + p_1)} \tag{2.4}$$

where σ_p and σ_n are the capture cross section for holes and electrons, while v_{th} is the thermal velocity of the charge carriers. n_1 and p_1 are statistical properties, defined as what the equilibrium electron and hole concentrations would be if the Fermi level of the material was at the defect energy level:

$$p_1 = p_i \, exp\left(\frac{-(E_t - E_i)}{k_B T}\right), \qquad n_1 = n_i exp\left(\frac{E_t - E_i}{k_B T}\right) \tag{2.5}$$

where p_i and n_i is the intrinsic concentration of holes and electrons, E_i is the intrinsic energy level, E_t is the defect energy level, k_{B} is the Boltzmann constant and T is the absolute temperature.

The electron and hole capture time constants τ_{n0} and τ_{p0} are given as:

$$\tau_{p0} = \frac{1}{\sigma_p N_t v_{th}}, \qquad \tau_{n0} = \frac{1}{\sigma_n N_t v_{th}} \tag{2.6}$$

Note that (2.4) describes a single defect level. The total SRH recombination rate will be a sum of all the defect levels at different energy levels throughout the silicon crystal such that $U_{\mathrm{SRH}} = \sum_{i=1}^{n} U_{\mathrm{SRH},i}$.

2.1.2 Surface recombination

The abrupt termination of the crystal lattice leaves a layer of unsaturated atoms at the surface which are highly reactive. These unsaturated atoms, often referred to as dangling bonds, introduce surface or interface states which contribute greatly to recombination losses. The surface recombination is mathematically like the SRH recombination, but because the surface is of two dimensions, contrary to the bulk's three dimensions, the lifetime defined in equation (1.1) cannot be applied. Hence, the surface recombination velocity (SRV), S, is introduced as:

$$\frac{1}{S} = \frac{\Delta n_s}{U_s} \tag{2.7}$$

where Δn_s is the excess carrier concentration at the surface and U_s is the surface recombination rate. By examining equation (2.7) it is clear that a high surface recombination rate $U_s$corresponds to a high

SRV, which means a high recombination activity at the surface. In comparison, a high recombination rate U in the bulk corresponds to a low carrier lifetime.

The surface recombination is mathematically similar to the recombination by defects in the bulk, but unlike the recombination via defects in the bulk, the introduced energy levels at the surface are not discrete and must be treated as a density distribution $D_{it}(E)$. Further, the recombination rate U_s is found by integrating the SRH recombination over the bandgap from E_v to E_c:

$$U_s = (n_s p_s - n_i^2) v_{th} \times \int_{E_v}^{E_c} \frac{D_{it}(E)}{\frac{n_s + n_1(E)}{\sigma_p(E)} + \frac{p_s + p_1(E)}{\sigma_n(E)}} dE \tag{2.8}$$

where n_s and p_s are the concentrations of electrons and holes at the surface respectively. Note that the capture cross sections $\sigma_p(E)$ and $\sigma_n(E)$, as well the statistical parameters $n_1(E)$ and $p_1(E)$ are now energy dependent. Further, it is common to simplify equation (2.8) by replacing the interface distribution $D_{it}(E)$ with a single, effective defect level with a concentration per area N_{it}. The rate of surface recombination is then given as:

$$U_s = \frac{S_{n0} S_{p0} \, (n_s p_s - n_i^2)}{S_{n0}(n_s - n_1) \; + \; S_{p0}(p_s - p_1)} \tag{2.9}$$

S_{n0} and S_{p0} are the surface recombination velocity parameters for electrons and holes defined as $S_{n0} = \sigma_n N_{it} v_{th}$ and $S_{p0} = \sigma_p N_{it} v_{th}$ respectively. These parameters reflect the density of interface states and the capture cross section of these states; a well passivated surface will have a small S_{p0} or S_{n0}.

2.2 Surface passivation

Based on Aberle (2000).

The goal of surface passivation is to reduce the recombination rate and thus to limit the SRV. By studying equation (2.8), which describes the mechanisms in the recombination rate, it is clear the recombination rate is proportional to the charge carriers at the surface (n_s and p_s) and the density of interface states (D_{it}). Surface passivation is therefore the process of reducing either of these parameters. There are two main strategies for doing this: *Chemical passivation* and *field effect passivation*. In practice, the techniques are often required to be applied together to achieve satisfying passivation.

2.2.1 Chemical passivation

Reduction of the interface states D_{it} is often referred to as chemical passivation. One of the methods, which are used in this study, is to dip the sample in a solution of hydrofluoric acid. This strips the sample of its inherent oxide layer and creates a hydrogenated surface, before a different material is deposited at the surface. The most common materials are amorphous, hydrogenated silicon (a-Si:H) and silicon nitride (a-SiN_x:H), using plasma enhanced chemical vapor deposition (PECVD). The hydrogen in these films will diffuse to the interface and saturate the dangling bonds.

2.2.2 Field effect passivation

The recombination rate is limited by the least abundant charge carrier (given equal cross sections), as recombination is dependent on the presence of both a hole and an electron. By reducing either one of the charge carriers, n_s or p_s, the surface recombination velocity, as well as the surface potential, will decrease. This procedure is called field-effect passivation. Field-effect passivation can be achieved by deposition of a dielectric containing fixed charges, Q_f, at the surface. This will create an electric field within the wafer as either the holes or electrons – depending on the polarity of the fixed charges – will be repelled. In addition to reducing the surface concentration, the fixed charges will create a pn-junction in the substrate which will act as a separator for the generated electron-hole-pairs. The concentration of the fixed charges in the dielectric determines the quality of the of the field effect passivation. Much work has therefore been done to determine Q_f of different materials. Other properties needed for a material to be suitable for passivation include thermal and electronic stability, suitable fabrication costs and production time. A further description of commonly used materials for surface passivation is found in chapter 2.5.

2.3 Band structure and charge distribution

Based on the work of Haug (2014).

The charge distribution in the silicon wafer is affected when a passivating dielectric layer is deposited on the surfaces. The energy bands are bending towards the energy bands of surface which reduces the charge carriers at the interface. Figure 2-1 shows the energy bands of a p-type substrate bending towards the interface.

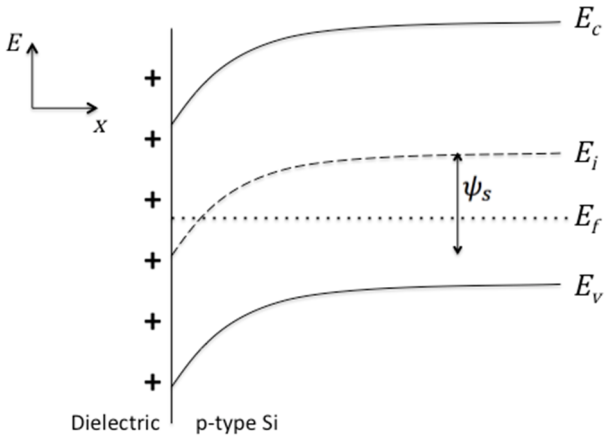

Figure 2-1: The energy bands bending towards the energy level of dielectric layer containing fixed, positive charges. ψ_s is the surface potential, which is the potential difference between the bulk and the surface.

2.3.1 Flat band condition

The flat band condition is the simplest case to describe surface recombination. In this case there are no electric charges present in the silicon, and thus the energy bands are flat. This also implies that the carrier concentration at the surface is equal to the concentration in the bulk such that $n_s = n$ and $p_s = p$ which simplifies equation (2.8) and (2.9) greatly. For a substrate with a passivating layer containing charges, the flat band condition is obtained by applying an extern voltage. The applied voltage must be equal the work function difference between the silicon and the metal gate and the fixed charges. This relationship is useful for determining fixed charges in passivation layers, for instance by a C–V sweep. This method will be further explained in chapter 3.3.1.

2.3.2 Surface band bending

When there are electrical charges present at the silicon surface, as with a dielectric passivation layer containing fixed charges, the energy bands will bend towards the surface, shown in Figure 2-1 because of the electric field present in the substrate, the carrier concentration at the surface is now highly different from the bulk. The recombination rate in equation (2.9), is now dependent on finding n_s and p_s. The starting point is finding the carrier concentration in the bulk of the semiconductor, n_b and p_b:

$$n_b = n_0 + \Delta n, \qquad p_b = p_0 + \Delta n \tag{2.10}$$

where n_0 and p_0 are the electron and hole concentration at thermal equilibrium. n_s and p_s can then be found by solving:

$$n_s = n_b e^{\beta\psi_s}, \qquad p_s = p_b e^{-\beta\psi_s} \tag{2.11}$$

where ψ_s is the surface potential, seen as the amount of band bending in Figure 2-1, while $\beta = \frac{q}{k_B T}$ where q is the elementary charge, k_B is the Boltzmann constant and T is the absolute temperature. Calculation of the effective SRV is thus reduced to determination of the surface potential.

2.3.3 Charge distribution and Girisch model

The Girisch model (Aberle 1999) is a good approximation solution to find the surface charge carriers and thus the SRV. Constant quasi-Fermi levels must be assumed throughout the space charge region, which is normally a good approximation for Si-passivation. The structure that is analyzed is shown in the upper part of Figure 2-2. The starting point of the analysis is the assumption of charge neutrality within the structure, such as:

$$Q_g + Q_f + Q_{it} + Q_{sc} = 0 \tag{2.12}$$

where Q_g is the charge in the metal electrode, Q_f is the fixed charge in the dielectric, Q_{it} is the charge associated with the interface states and Q_{sc} is the charge in the space charge region. The charge distribution is illustrated in the lowermost part of Figure 2-2.

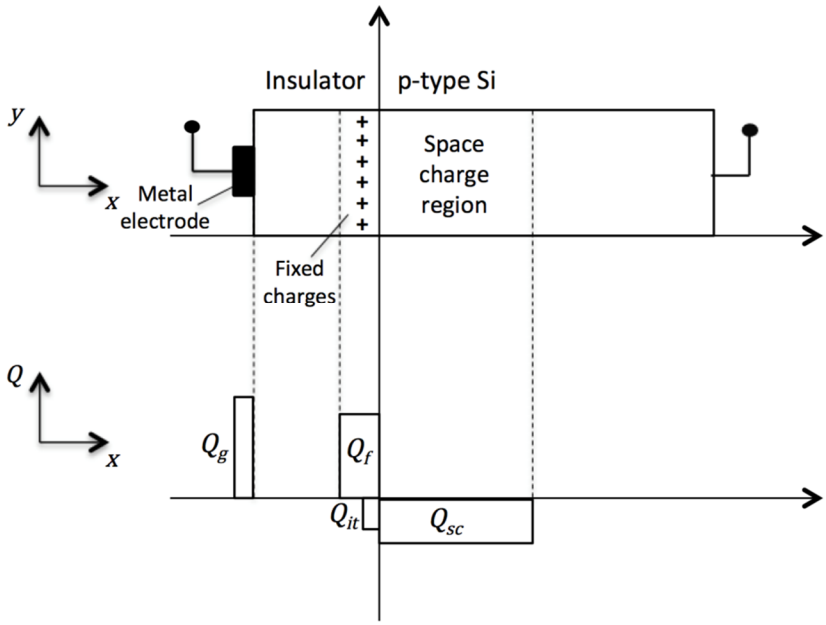

Figure 2-2: The uppermost figure shows the physical layout of the MIS-structure, while the lowermost figure shows the charge distribution in the structure containing fixed, positive charges.

The gate charge Q_g is given by:

$$Q_g = \frac{\varepsilon_0 \varepsilon_i}{d_i q}\left(V_g + \Delta\phi_{ms} - \psi_s\right) - \frac{Q_f d_f}{2 d_i} \tag{2.13}$$

where ε_0 is the permittivity of vacuum, ε_i is the relative permittivity of the insulator, d_i is the thickness of the insulator and q is the elementary charge, note that the first term, which includes these parameters, $\left(\frac{\varepsilon_0 \varepsilon_i}{d_i q}\right)$, corresponds to the insulator capacitance per area. Further is V_g the gate voltage, d_f the thickness of the region containing fixed charges, ψ_s is the surface potential and $\Delta\phi_{ms}$ is the metal-semiconductor work function difference. For a p-type sample $\Delta\phi_{ms}$ is calculated as:

$$\Delta\phi_{ms} = F_m - \chi_{Si} - \frac{E_g}{2} - \frac{k_B T}{q} ln\left(\frac{N_A}{n_i}\right) \tag{2.14}$$

where χ_{Si} is the electron affinity of Si ($\chi_{Si} = 4.05$ eV), F_m is the metal work function for aluminum ($F_m = 4.1$ eV). The work function difference $\Delta\phi_{ms}$ for a sample with resistivity of 2.8 Ωcm is thus –0.84 V.

The fixed charge concentration in the insulator, Q_f, can be measured by a capacitance-voltage measurement. This method will be further explained in chapter 3.

The charge associated with the space charge region, Q_{sc}, can be found by:

$$Q_{sc} = \pm\sqrt{\frac{2n_i\varepsilon_0\varepsilon_s}{q\beta}\left(e^{\beta(\phi_p-\psi_s)} - e^{\beta\phi_p} + e^{\beta(\psi_s-\phi_n)} - e^{-\beta\phi_n} + \beta\psi_s\frac{N_A-N_D}{n_i}\right)} \tag{2.15}$$

where ϕ_n and ϕ_p and are the quasi-Fermi levels for electrons and holes respectively. The minus sign in equation (2.15) corresponds to $\psi_s > 0$ and plus for $\psi_s < 0$.

By assuming that the charge associated with the interface states Q_{it} is negligible, the surface potential can be calculated using equation (2.12), (2.13) and (2.15).

2.4 Effective lifetime

Based on the work of Sproul (1994).

All lifetime measurements yield the effective lifetime τ_{eff}, which is composed of two components: The recombination in the volume of the sample, and the recombination that occurs at the surfaces:

$$\frac{1}{\tau_{eff}} = \frac{1}{\tau_b} + \frac{1}{\tau_s} \tag{2.16}$$

where τ_b is the bulk lifetime and τ_s is the surface lifetime. As equation (2.16) shows, the mechanism with the highest recombination rate, and thus the lowest lifetime, will be dominating.

The bulk lifetime is a combination of the three bulk recombination mechanisms, such that $U_b = U_{\mathrm{rad}} + U_{\mathrm{Aug}} + U_{\mathrm{SRH}}$ and further $\tau_b = \frac{\Delta n}{U_b}$. The surface lifetime depends on the SRV of the front and back surfaces, S_f and S_b, which may have different values. The general solution of τ_s is carried out by considering the boundary conditions for the second order differential equation, which describes the carrier decay:

$$\frac{1}{\tau_s} = \alpha_0^2 D \tag{2.17}$$

where *D* is the diffusion coefficient and α_0 is the smallest eigenvalue solution of:

$$tan(\alpha_0 W) = \frac{S_f + S_b}{\alpha_0 D - \frac{S_f S_b}{\alpha_0 D}} \tag{2.18}$$

where W is the thickness of the substrate. Equation (2.18) must be solved numerically.

For a sample where the surfaces are equally passivated, such that the surface velocities can be assumed to be equal ($S_f = S_r = S$), and S is small eq. (2.17) can be simplified to:

$$\frac{1}{\tau_s} = \frac{2S}{W} \tag{2.19}$$

and further the effective lifetime is found by solving:

$$\frac{1}{\tau_{eff}} = \frac{1}{\tau_b} + \frac{2S}{W} \tag{2.20}$$

However, τ_b is usually unknown. To obtain S from experiments where τ_{eff} is obtained, the calculations often yield S_{max}, as an upper limit, by assuming infinite bulk lifetime. S_{max} is thus calculated as:

$$S_{max} = \frac{W}{2\tau_{eff}} \tag{2.21}$$

2.5 Materials used for surface passivation

In this chapter a variety of different materials and their properties are presented. As described in the previous chapter, a combination of both good chemical passivation and field effect passivation is desired for the passivation material. Amorphous silicon (a-Si) is widely used for passivation of silicon solar cells. a-Si provides a good chemical passivation, but unlike the other materials presented, a-Si is not a dielectric material and does not contain any fixed charges, and thus offers poor field-effect passivation. The materials passivation characteristics are normally classified in term of the material's interface state density (D_{it}), its concentration of fixed charges (Q_f), its thermal stability and its refractive index. Production costs are also normally considered.

2.5.1 Thermal silicon oxide

The following discussion of thermal oxide is based on Aberle (2000) and Haug (2014).

Thermal oxidation at high temperatures (~1000 ℃) has been the standard method for passivation of Si surfaces for many years. The growth of the SiO_2 layers into the c-Si surface provides an efficient passivation layer, especially for high resistivity substrates (>100 Ωcm) with surface state densities as low as $\sim 10^{-9}$ $cm^{-2}eV^{-1}$. However, for low resistivity substrates (~1 Ωcm), the passivation effect depends on the doping type. While the passivation quality is good for n-type wafers, it is significantly poorer for p-type substrates. Moreover, thermal silicon oxide provides a moderate field-effect passivation caused by fixed charges located at the interface, usually with a density in the range $1\text{-}5\times 10^{11}$ cm^{-3} (Mack et al. 2011). In addition to the problems with low-resistivity, thermally grown SiO_2 suffers from some severe drawbacks (Aberle 1999). The surface passivation is unstable when exposed to the UV-photons of sunlight, and does not provide the high surface passivation in these conditions. Another problem is the small refractive index (1.46) that makes SiO_2 a poor anti reflection coating. Other complications arise with the high processing temperature (1100-1200 ℃) that is required to yield the lowest D_{it}. The metal contacts cannot be deposited prior to the high temperature process as this will degrade the bulk carrier lifetime and the metal will penetrate the emitter and destroy the pn-junction. This makes the production cumbersome, costly and time consuming.

2.5.2 Silicon nitride

The theory of silicon nitride is based on the work from Aberle (2001) and (Schmidt et al. 2001) .

Amorphous silicon nitride is a dielectric that has been used for a large variety of electronic components. The silicon nitride is almost always processed by plasma-enhanced chemical vapor deposition (PECVD). This method uses hydrogen-containing reactants, resulting in a non-stoichiometric silicon nitride with up to 40 atomic percentage of hydrogen. The film is therefore most precisely referred to as a-SiN_x:H, but is usually shortened to SiN_x, where x denotes the nitrogen/silicon atomic ratio. The ratio of Si and N affects the electronic and optical properties largely. One general trend from the literature is that the best passivation usually is achieved with Si-rich films. Si-rich films provide moderate fixed charge density, but a high degree of chemical passivation. N-rich films have a better chemical and thermal stability and usually a higher density of fixed charges (in the order of $\sim 10^{12}$ cm^{-2} (Haug 2014)) and thus give a higher field-effect. Effective SRV as low as 4 cm/s have been reported on nitride rich film deposited on low resistivity substrate (Schmidt et al. 1996). Additionally, the refractive index of SiN_x has proved to be suitable, with $n = 1.8$ (Haug 2014), and upwards, depending upon the ratio of precursors gas flow.

There exists a very thin layer (∼2 nm) of SiO_2 at the Si – SiN_x interface. This layer occurs due to air exposure in the time period between when the substrates are loaded into the deposition chamber and the deposition starts. This results in a possibility of O, N and H bonding with unsaturated Si-atoms at the Si – SiN interface. Si-atoms back bonded with three oxygen atoms, P_{ox} defects, contributes with $\sim 1 \times 10^{11}$ elementary charges per cm^2. However, the dominating defects are Si-atoms back bonded to three nitrogen atoms, called K-centers (Aberle 1999). The K-centers can be negatively, neutrally or positively charged. A ∼20 nm thick layer of positively charged K-centers is found at the Si – SiN_x interface, which contributes to the good field-effect passivation provided by nitride films. However, the K-centers are not stable, UV-illumination may neutralize the positive K-centers. The K-centers are most stable in the negative (K^-) or positive (K^+) state. The neutral K-centers (K^0) will thus return to their stabile positive charge upon termination of the UV-illumination. The changing of charge state is mostly observed as large hysteresis effects in a C–V measurement.

2.5.3 Stacks

Based on the work of Cheng et al. (2016) and Haug (2014).

The single layer passivation techniques described above can be used in stack systems where the properties of the individual layers are combined. The structure is normally organized such that the bottom layer, which is in direct contact with the silicon crystal, has a low defect concentration and a high concentration of hydrogen to passivate the dangling bonds. For the capping layer is properties such as low absorption, high concentration of fixed charges, good thermal stability is desirable. Different materials and deposition techniques has been studied, such as amorphous silicon with capping layers of aluminum oxide or silicon nitride.

The surface state density of PECVD nitrides is much larger than the thermally grown oxide, while the field effect passivation is much better for the nitride. These properties are suitable for stack purposes, where an oxide layer is deposited as a buffer layer, and nitride used for capping layer.

CHAPTER 3

INTRODUCTION TO CHARACTERIZATION METHODS

This chapter presents the experimental methods used for characterization of the passivation films. The chapter is divided in three parts: Optical properties, lifetime measurements and characterization under applied bias.

Section 3.1 presents the ellipsometry method. The ellipsometry is used to measure the refractive index and thickness of the dielectric films, which is further used to estimate the reflection of the samples.

Section 3.2 discusses methods for lifetime measurements and is divided in two parts. 3.2.1 presents the quasi-steady state photoconductance (QSSPC), which measures the effective lifetime based on the change of photoconductance. Section 3.2.2 presents photoluminescence imaging (PL–I), which is used to evaluate the spatial quality of the samples.

Section 3.3 presents two experimental methods used for charging the dielectric films. In section 3.3.1 is the capacitance–voltage (C–V) method explained. This method is used to establish the flatband voltage, to quantify the charges present in the film. Section 3.3.2 describes the photoluminescence-voltage (PL-V). This technique uses photoluminescence imaging in combination with an applied bias to monitor the effective lifetime as a function of altering voltage. Simulations of the experimental data are conducted using the Girisch model. This quantifies parameters such as the fixed charge density and the effective surface recombination parameters for holes and electrons.

3.1 Optical properties

3.1.1 Variable angle spectroscopic ellipsometry

Variable angle spectroscopic ellipsometry (VASE), or just ellipsometry, is a technique used to measure several different properties of dielectrics. In this work, ellipsometry is used to measure the thickness and the refractive index of the dielectric film deposited on the silicon surface. The setup, consisting of a light source, a monochromator and a polarizer on the left-hand side of the stage, and an analyzer and a detector on the right-hand side, can be seen in Figure 3-1. The monochromator determines the desired wavelength, and the waveplate alters the polarization. The polarized light that hits the sample is reflected differently according to the incident plane, which is either in the s-plane (parallel to the sample surface) or in the p-plane (normal to the surface). The reflection ratio between the s-plane, R_s, and the p-plane, R_p, is expressed in terms of the ellipsometric parameters as:

$$\frac{R_p}{R_s} = \tan(\Psi)e^{i\Delta} \tag{3.1}$$

where Ψ and Δ are the spectroscopic parameters, which reflects the amplitude ratio of the reflected beam and the phase shift respectively.

To describe the sample after it is measured, an optical model is constructed. The best match between the experimental data and the model is usually obtained by regression. The validity of the analysis is thus dependent on the accuracy of the model, as well as the physical properties of the instrument.

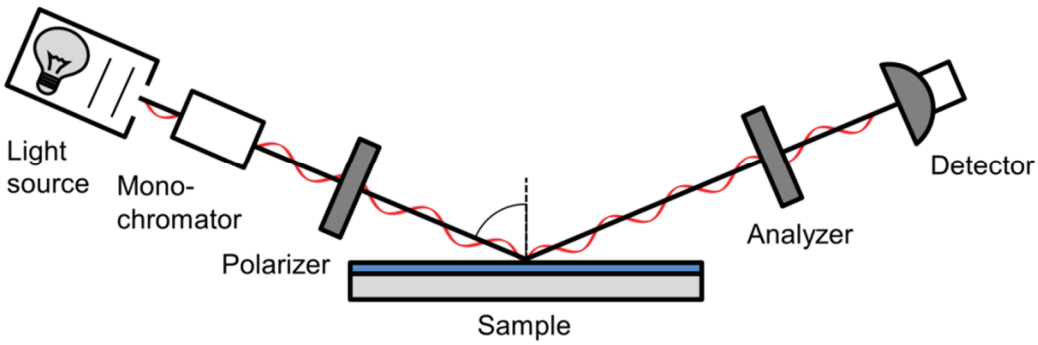

Figure 3-1: Schematic setup of the variable angle spectroscopic ellipsometry. Figure from Haug (2014).

3.2 Lifetime measurements

3.2.1 Quasi-steady state photo conductance

The following section is based on the work of Sinton et al. (1996), Nagel et al. (1999) and Cuevas and Macdonald (2003).

Quasi-steady state photoconductance (QSSPC) is a technique where the excess carrier concentration is calculated from measuring the conductivity of the sample under illumination. The setup consists of a light source located vertically over the stage with an inductively coupled coil connected to an RF-bridge. A schematic view of the setup is shown in Figure 3-1. the inductively coupled coil is used to measure the increase in photoconductance when the sample is illuminated. The change of photoconductance is then used to calculate the excess carrier concentration, which again is used to estimate the effective lifetime. In this manner, the lifetime is measured as a function of injection level, where the user determines the time constant for the flash lamp.

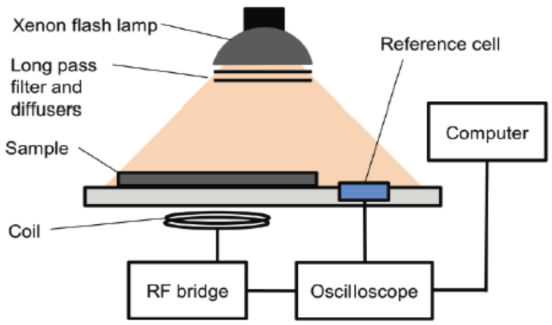

Figure 3-2: A schematic view of the QSSPC setup. Figure from Haug (2014).

The first design of the setup required a long illumination time, such that the generation and the recombination rate was in balance at all time. This mode is especially useful for samples with short lifetime. However, samples with longer lifetimes are best measured using shorter time constants for the flash lamp. A generalized analysis was developed, which allows for measurements using both long and short time constants on the same setup. A short light pulse leads to a quasi-transient measurement, while a longer light pulse results in a quasi-steady-state measurement.

The starting point for the generalized analysis procedure is the continuity equation for the excess charge density:

$$\frac{\partial \Delta n(t)}{\partial t} = G(t) - U(t) + \frac{1}{q}\nabla J \tag{3.2}$$

where G is the generation rate, U is the recombination rate, q is the elementary charge and J is the electron current density. The sample is uniformly illuminated such that a homogeneous generation throughout the wafer can be assumed. The gradient current in equation (3.2) can thus be omitted with a small error. By substituting the generation rate given in equation (2.1), equation (3.2) may be rearranged as:

$$\tau_{eff}(\Delta n) = \frac{\Delta n(t)}{G(t) - \frac{\mathrm{d}\Delta n(t)}{\mathrm{d}t}} \tag{3.3}$$

Finding the effective lifetime τ_{eff} is then a matter of finding the time dependent generation rate, $G(t)$, and the time dependent excess carrier concentration, $\Delta n(t)$.

The setup measures the change in photoconductance, $\Delta\sigma(t)$, which is given as:

$$\Delta\sigma(t) = q\Delta n(t)\big(\mu_n + \mu_p\big)W \tag{3.4}$$

where W is the wafer thickness, and μ_n and μ_p are the mobility of electrons and holes respectively. The mobilities are a function of carrier density and temperature and can be found in the literature. Equation (3.4) can be used to calculate $\Delta n(t)$ when the photoconductance is known.

The generation rate, $G(t)$, is measured using a reference cell, given as (Haug 2014):

$$G(t) = OC \times \frac{I_{\mathrm{ref}}(t)}{qW_{\mathrm{ref}}} \tag{3.5}$$

where I_{ref} is the measured photocurrent, W_{ref} is the thickness of the reference cell, and OC is the optical constant which is determined by the optical properties of the reference cell compared to the reference diode.

The quasi-steady state and the quasi-transient mode are two limiting cases for equation (3.3). While the generation rate is approximately constant for the steady state mode ($G(t) \gg \partial\Delta n/\partial t$), the opposite is true for the transient mode ($G(t) \ll \partial\Delta n/\partial t$). This results in the following simplifications of equation (3.3) for the effective lifetime:

$$\tau_{eff,\text{steady-state}}(\Delta n) = \frac{\Delta n(t)}{G(t)} \tag{3.6}$$

and

$$\tau_{eff,\text{transient}}(\Delta n) = -\frac{\Delta n(t)}{\frac{\partial \Delta n}{\partial t}} \tag{3.7}$$

The measurement can then be repeated with different time constant until the output data is satisfying. Figure 3-3 shows a lifetime versus excess carrier density obtained from a QSSPC measurement.

The QSSPC measurement does not provide spatial information about the sample; the measurements are limited to the coil area, which is usually ~2 cm^2. A photoluminescence-imaging (PL-I) setup is used to determine the spatial quality of the sample, and thus the validity of the QSSPC measurements. PL-I is further explained in the following section.

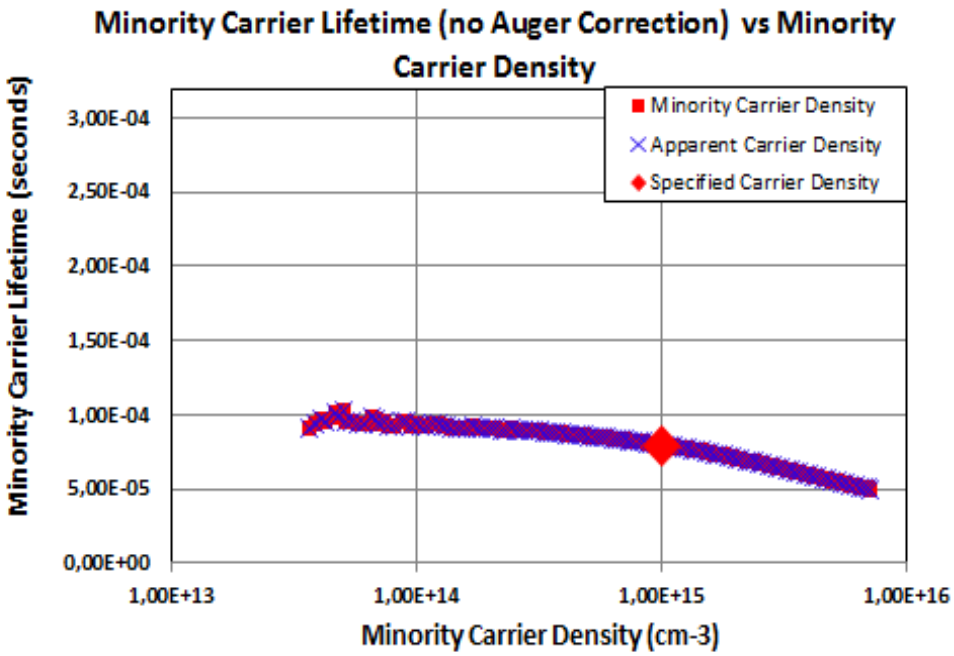

Figure 3-3: A lifetime versus carrier density curve of sample 2 obtained from QSSPC.

3.2.2 Photoluminescence Imaging (PL-I)

The following description of PL-I is based on theory from Trupke et al. (2012), Haug (2014) and Herlufsen et al. (2008).

Photoluminescence imaging is a fast and contactless technique, which yields a spatial resolution of the sample quality. The surface of the samples is exited to emit luminescence, and a camera detects the luminescence emission. The setup consists of a laser with a wavelength of 808 nm, placed diagonally over the stage where the sample is mounted, and a charge-coupled device (CCD) sensor vertically over the sample. Figure 3-4 shows the setup. The PL-I technique is based on radiative recombination, described in chapter 2.1.1, where the excess energy in the recombination is released as a single photon. The sensor detects the photons, such that the resulting image yields a spatial resolution of the sample where each pixel corresponds to the number of photons detected from one particular area. An integrated QSSPC setup can be used to calibrate the measurement such that the pixels are given as the effective lifetime.

Figure 3-5 shows a photoluminescence image of one of the samples used in this study. This is an uncalibrated picture where the scale is of arbitrary units. It is clear from the image that the sample has some defects in the upper part and around the edge of the sample.

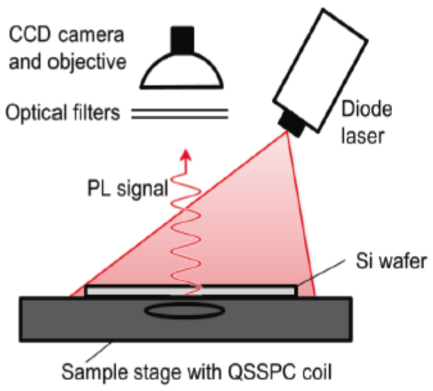

Figure 3-4: A schematic setup of the camera based photolumeniscence technique. Figure from Haug (2014).

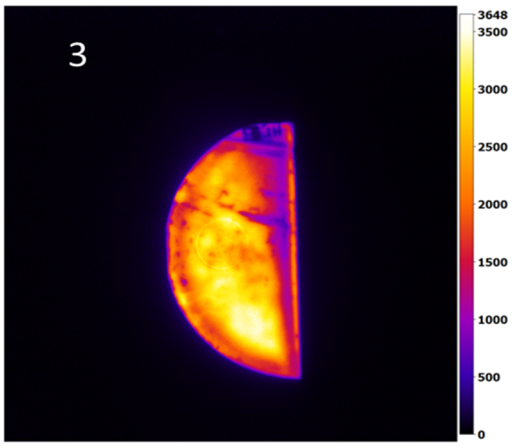

Figure 3-5: A PL-I of sample 3 used in this study. The image is uncalibrated such that the scale is of arbitrary units. Studying this image shows defects in the upper part of the sample, as well as along the edges.

As each photon from the incident light creates one electron–hole pair, the detected photointensity ϕ_{PL}, is similar to U_{rad} from equation (2.2):

$$\phi_{PL} = B_{\mathrm{rad}}(np - n_i^2) \tag{3.8}$$

By assuming a moderately doped sample, such that $p = N_A + \Delta n$ and $\cong \Delta n$, the photocurrent intensity, I_{PL}, is given as:

$$I_{PL} = C_{\mathrm{cal}} B_{\mathrm{rad}}(N_A + \Delta n)\Delta n \tag{3.9}$$

where C_{cal} is a calibration constant based on the amount of light detected by the camera. This constant can be found using an integrated QSSPC measurement. However, because of a high uncertainty of the correctness of the integrated QSSPC setup is an external QSSPC setup used for calibration in this study. Data from the injection dependent lifetime graph, shown in Figure 3-3 is extracted and further is C_{cal} is determined using equation (3.9). I_{PL} is obtained from the PL-I measurement and Δn from the QSSPC measurement, such that $\Delta n = \Delta n_{QSSPC}$.

The excess carrier concentration at each point, $\Delta n(x, y)$, is found by rearranging equation (3.9):

$$\Delta n(x, y) = \sqrt{\left(\frac{N_A}{2}\right)^2 + \frac{I_{PL}(x, y)}{C_{\mathrm{cal}} B_{\mathrm{rad}}}} - \frac{N_A}{2} \tag{3.10}$$

The PL-I is measured under steady state conditions such that the recombination rate equals the generation rate. The expression for τ_{eff} given in equation (2.1) can then be rearranged for a specific point in the image, $\tau_{eff}(x, y)$:

$$\tau_{eff}(x, y) = \frac{\Delta n(x, y)}{G} \tag{3.11}$$

where G is the generation rate given as:

$$G = \frac{(1 - R_f)\phi_{PH}}{W} \tag{3.12}$$

where R_f is the refractive index at 808 nm, ϕ_{PH} is the photon flux from the light source and W is the thickness of the sample.

3.3 Measurements under applied bias

3.3.1 Capacitance–voltage (C–V) measurements

The following section is based on theory from Schroder (2006) and Aberle (1999).

The main motivation for the capacitance-voltage (C–V) measurement is to obtain a precise measurement of the fixed charge Q_f. The samples are turned into metal-insulator-semiconductor (MIS) structures by depositing aluminum contacts on the front and the rear side where the gate voltage is applied. Figure 3-6 shows the setup. The measurement is carried out by slowly varying an applied DC-voltage to the MIS-structure so that it is driven from accumulation to inversion. A small AC-signal is superimposed to the probe where the charge variation gives rise to the capacitance. The flat band voltage is observed as a shift along the voltage axis and is further used to estimate the fixed charge.

The definition of capacitance, C, is the change in stored charge due to a change in voltage. Seen from the gate of a MIS-structure the capacitance is:

$$C = q\frac{dQ_g}{dV_g} \tag{3.13}$$

where Q_g is the gate charge and V_g is the gate voltage.

The structure consists of a metal contact where the voltage V_g is applied, the insulator and the semiconductor. Figure 3-7 shows an equivalent circuit of the structure. The capacitance of the semiconductor is a parallel connection between the capacitance associated with the interface states and the space charge region. The total capacitance, C_{tot}, of the structure is given as:

$$\frac{1}{C_{\mathrm{tot}}} = \frac{1}{C_i} + \frac{1}{C_{sc} + C_{it}} \tag{3.14}$$

where C_i is the capacitance of the insulator, while the last term is the capacitance in the semiconductor, C_{sc} for the space charge region and C_{it} is the capacitance for the interface states.

The total charge in the device must be zero and the applied voltage is therefore dropped partially over the insulator and the semiconductor:

$$V_g = V_{fb} + V_i + \psi_s \tag{3.15}$$

where V_{fb} is the flat band voltage, V_i is the insulator voltage and ψ_s is the surface potential.

The charges in the insulator layer are fixed such as the insulator may be seen as a perfect plate-capacitor where no electric current is conducted. The capacitance is thus independent of the applied voltage and may be calculated as:

$$C = \frac{\epsilon_i \epsilon_0 A}{d} \tag{3.16}$$

where ϵ_i is the relative permittivity of the insulator, ϵ_0 is the permittivity in vacuum, and d and A are the thickness and area of the insulating layer respectively.

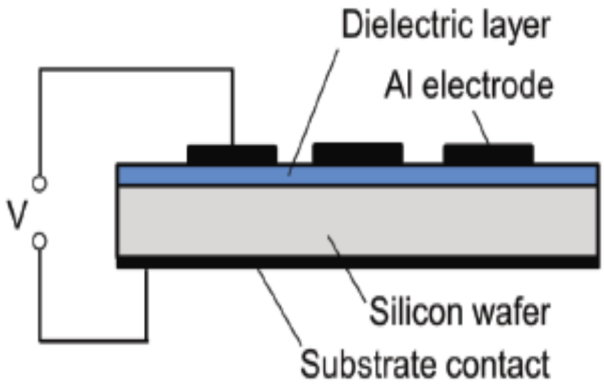

Figure 3-6: Schematic illustration of the C–V setup. Figure from Haug (2014)

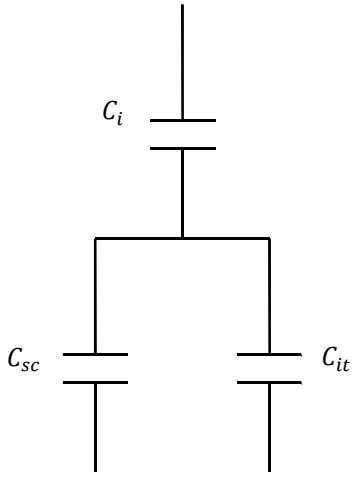

Figure 3-7: Equivalent circuit of the MIS-structure.

Unlike the insulator, applying a gate voltage alters the concentration of charge carriers in the semiconductor. This causes the energy bands to bend. However, the fermi level must remain flat as long as the insulator is assumed to be perfect. This will thus affect the charge concentration and consequently the capacitance. During a C–V measurement, the gate voltage is driven from positive to negative values where the capacitance is measured for each step. shows an ideal curve for a C–V measurement. The further descriptions of the stages during a C–V measurement are based on a p-type semiconductor.

Accumulation takes place when a large negative voltage is applied on the gate. The positive majority carriers in the semiconductor attract the negative applied voltage; the surface potential is of negative value and the positive carriers are accumulated at the surface. The spacing between the carriers in the semiconductor and insulator is minimized, leading to a very large semiconductor capacitance. The total capacitance approaches the insulator capacitance such that $C = C_i$.

Depletion happens when the applied gate voltage is increased towards positive values. The p-type silicon near the surface becomes ionized, leading to a negative space charge region. The width of the space charge region is increasing with increasing positive gate voltage, which leads to a decreasing semiconductor capacitance, and thus a reduction of the total capacitance.

Inversion occurs when the applied voltage is approaching positive values. The capacitance in inversion depends on the frequency of the probe signal. If the frequency is low enough, the minority carriers in the inversion layer is able to follow the AC-signal. The capacitance is thus reduced to C_i. For high frequencies, the inversion layer charge is unable to follow the applied signal and the total capacitance is a serial connection of C_i and C_{sc}. C–V measurements are most easily interpreted at high frequencies.

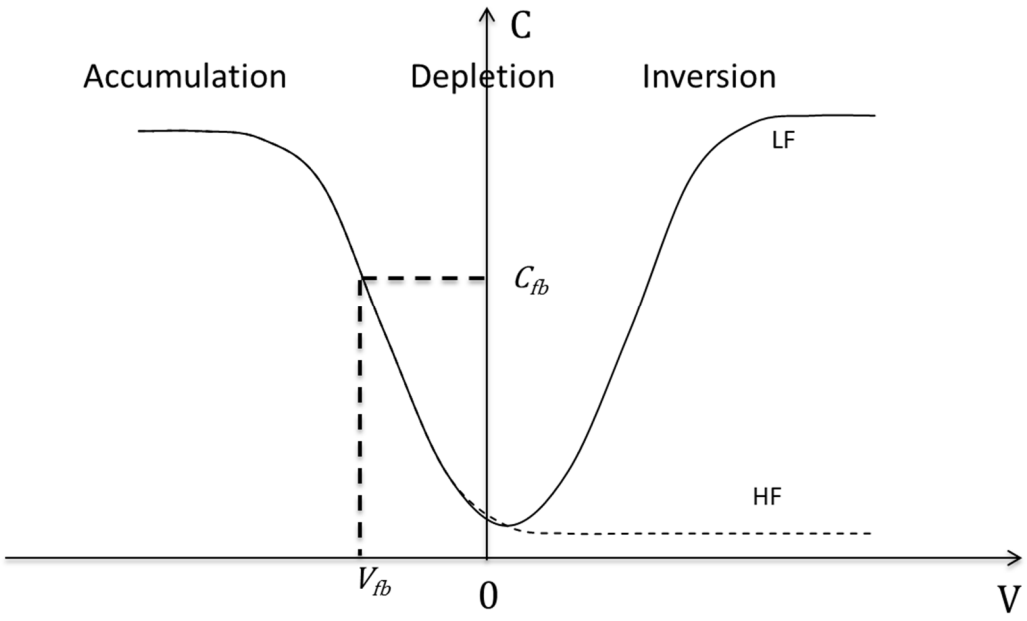

Figure 3-8: C–V plot of an MIS-structure with fixed charges.

3.3.1.1 FIXED CHARGE CALCULATIONS

In a C–V curve, the point where the surface potential is zero and thus the energy bands in the semiconductor flat is seen as a shift along the capacitance axis. The voltage applied at this point, the flatband voltage V_{fb}, and the corresponding capacitance, is essential for calculating the fixed charge density Q_f. The flatband capacitance in the semiconductor can be extracted either from the measurement, or be calculated using a simplified version of equation (3.14) where C_{it} is assumed to be small compared to C_{sc} and thus can be omitted. The space charge capacitance at flatband, $C_{sc,fb}$, can be calculated as:

$$C_{sc,fb} = \frac{\epsilon_{Si}\epsilon_0}{L_D} \tag{3.17}$$

where ϵ_{Si} is the relative permittivity of silicon and L_D is the Debye-length, which describes the screening depth in the silicon, calculated as:

$$L_D = \sqrt{\frac{k_B T \epsilon_{Si}\epsilon_0}{q^2 N_A}} \tag{3.18}$$

The flatband capacitance can then be calculated using equation (3.14), where $C_{TOT} = C_{fb}$.

The fixed charge density, Q_f, is then be calculated by solving the charge neutrality from equation (2.12) for Q_f. The gate charge, given in equation (2.13), is calculated by setting the surface potential, ψ_s, and the space charge density, Q_{sc}, to zero, which apply under flatband. Further simplification can be achieved by assuming that the fixed charges is located at the surface, such that $d_f = 0$ and assuming that the interface charge Q_{it} is small compared to Q_f and therefore negligible. The expression for the fixed charge is then given as:

$$Q_f = \frac{C_i}{q}(\Delta\phi_{ms} - V_{fb}) \tag{3.19}$$

3.3.2 Photoluminescence under applied bias (PL-V)

This section is based on the work of Haug et al. (2012) and Haug et al. (2014), where a new characterization technique is presented.

In this work, the PL-I setup described in chapter 3.2.2 is combined with an external bias applied on the rear dielectric film to control the density of charge carriers at the surface. Figure 3-9 shows a schematic illustration of the setup. Figure 3-10 shows a region of a sample under applied bias. The counts detected in the region depend on the voltage. Voltages close to V_{fb} results in a darker region, which is consistent with the principle of no band bending, and thus a high SRV at flatband. Analysis of the PL-V results allows for precise estimations of important parameters such as the fixed charge density and the effective surface recombination parameters, and consequently the capture cross sections, for electrons and holes.

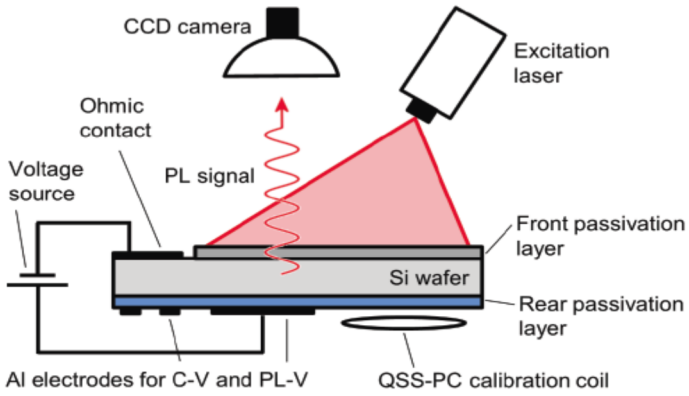

Figure 3-9: Schematic illustration of the PL-V setup. Figure from Haug (2014)

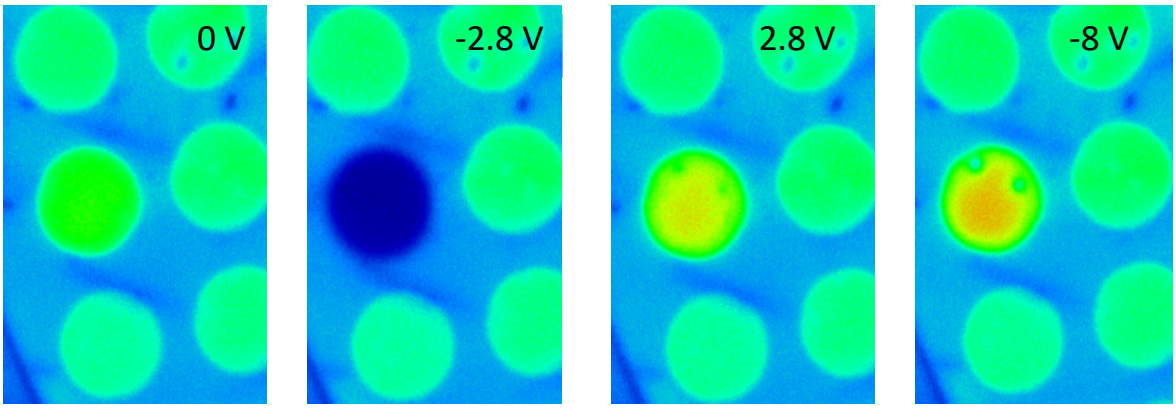

Figure 3-10: A region of a sample under applied bias measured with PL-V.

The modulation of the band bending in the semiconductor is of high importance for characterization purposes. Modulation of band bending can either be achieved by applying voltage on the dielectric film or by placing charged ions at the sample surface in a corona discharge chamber. The latter technique has been the main strategy for surface modulation for a long time, mainly because this measurement is contactless, and therefore non-invasive. However, this technique is time consuming and normally results in few measuring points. The PL-V technique requires metal contacts, but is in return highly effective. The method allows for fast measurements, simultaneously with data collection. The PL-V technique also facilitates repetitive sweeps, which enlighten the repetitiveness and voltage influence of the sample. The use of metal contacts will influence the measurement, as they will reflect more of the incident light. However, including a correction factor in the analysis can account for this.

The measurement is conducted by alternating the applied bias from positive to negative values, starting from zero, to minimize the influence from previous charges. The results obtained from such a measurement is the amount of counts detected at the region of interest, which can be calibrated to τ_{eff}, using the same method as explained in section 3.2.2. The squares in Figure 3-11 shows the results of a voltage sweep of sample 2 from -10 V to 10 V, where the effective lifetime is plotted as a function of applied voltage. The SRV as a function of gate voltage can be calculated from the obtained τ_{eff} data. The squares in Figure 3-12 are the SRV corresponding to τ_{eff} in Figure 3-11. The blue line in Figure 3-11 and Figure 3-12 is a simulation of the data, obtained by using of the Girisch model.

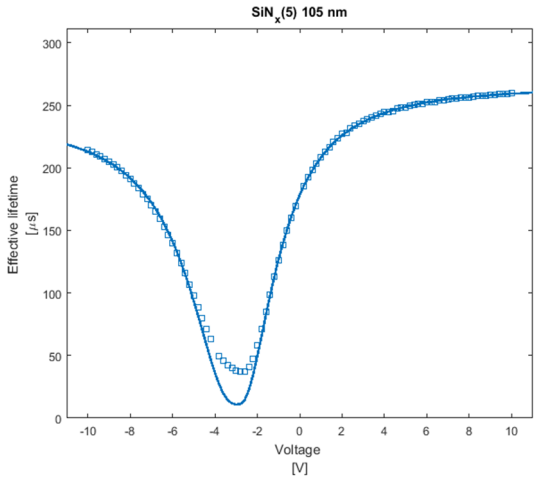

Figure 3-11: Effective lifetime obtained from the PL-V measurement is plotted as a function of applied voltage.

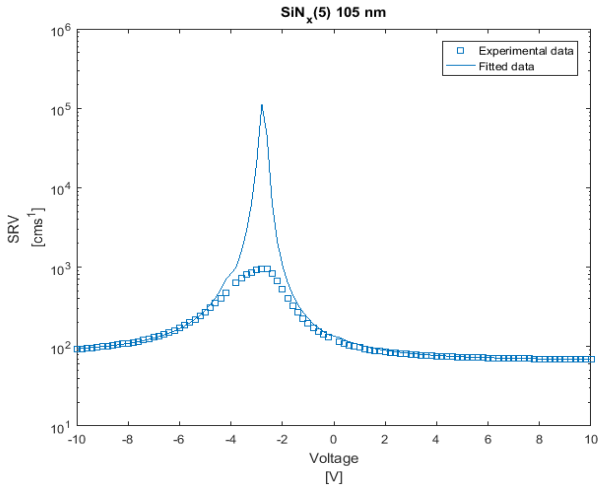

Figure 3-12: Surface recombination velocity as a function of applied voltage, measured by PL-V.

The simulation uses input parameters to optimize the free fitting parameters to approach a model that is in accordance with the experimental data. Table 3-1 shows the parameters used for fitting. A well-fitted model returns reliable data on the fixed charge density and the effective surface recombination parameters.

Fixed charge density	Q_f
Effective surface recombination parameter for electrons	S_{n0}
Effective surface recombination parameter for holes	S_{p0}
Minimum SRV for electrons for $\psi_s < 0$	$S_{\min,n}$
Minium SRV for holes for $\psi_s > 0$	$S_{\min,p}$

Table 3-1: Free fitting parameters used for the PL–V analysis.

The fixed charge Q_f is calculated from the minimum τ_{eff}, where the applied voltage equalizes the fixed charges and the metal–semiconductor work difference such that $\psi_s = 0$.

The minimum SRV parameters for electrons and holes, $S_{\min,n}$ and $S_{\min,p}$, are included to account for flattening of τ_{eff} at the highest and lowest voltages. A small $S_{\min,n}$ would mean flattening at a lower point towards accumulation.

The effective recombination parameters decide the slope on each side of the minimum τ_{eff}. A steep slope is expected for a material with high chemical passivation. A nitride rich SiN_x film provides poor chemical passivation, and is thus expected to have high effective recombination parameters and a less steep slope.

The capture cross ratio of electrons and holes, σ_n/σ_p is equal to S_{n0}/S_{p0}. This ratio describes the symmetry of the curve. A ratio of 1 gives a symmetrical curve around $\tau_{eff,\min}$, while a ratio different from 1 will cause differences in SRV towards accumulation and inversion.

Figure 3-13 shows the properties of each variable in the simulation. The simulation in Figure 3-13 is based on a sample where $S_{p0} = S_{n0}$ and $S_{\min,n} = S_{\min,p}$, while Q_f is set to zero. The curve is thus symmetrical around the minimumτ_{eff}. $\tau_{eff,\min}$ is found at –0.87 V, which corresponds to the metal–semiconductor work difference.

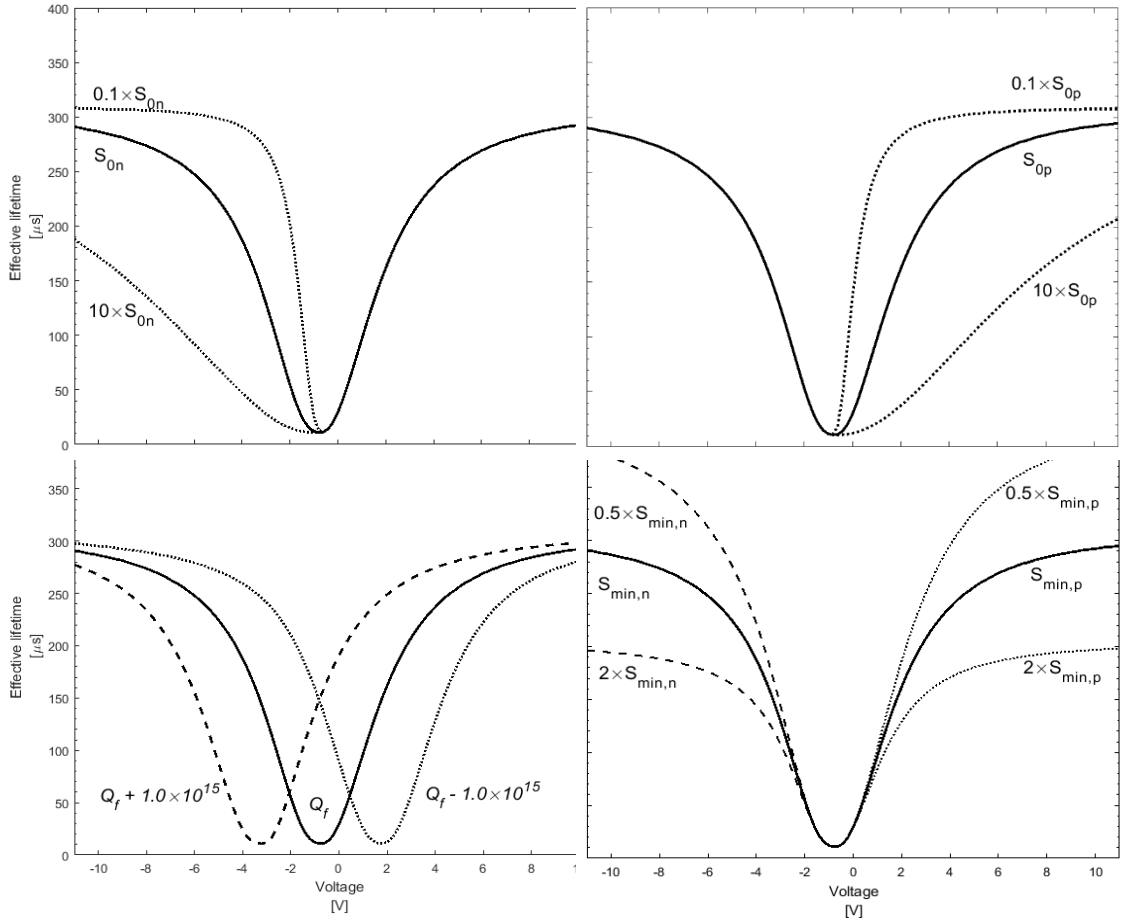

Figure 3-13: Properties of the free fitting variables used for the PL-V simulation.

A MATLAB-script developed by Halvard Haug has been used for optimizing the free input parameters to the experimental results.

CHAPTER 4

EXPERIMENTAL METHODS

This chapter presents the experimental execution, and is divided in two main parts.

Section 4.1 presents the substrate used and the design of the sample set. Further is preparation and fabrication of the samples explained, which includes deposition parameters, electrode metallization and annealing of the samples.

Section 4.2 presents the characterization execution. This includes the methods explained in chapter 3 and the equipment used in the experiments.

4.1 Sample processing

4.1.1 Sample preparation

Monocrystalline polished float zone p-type silicon wafers were used as substrates for the film deposition. Table 4-1 summarizes the wafer specifications used for film deposition.

Manufacturer	Topsil
Fabrication method	Float zone
Diameter	4 inches
Average thickness	280 $\pm$ 25 µm
Average resistivity	1–5 Ωcm
Crystal orientation	[100]
Doping	Boron
Average doping level	2.5×10^{15} – 1.5×10^{16} cm^{-3}

Table 4-1: Specifications sample substrates.

Any wafer exposed to air will form an oxide layer on the surface. To remove this layer, the samples were immersed in a 5% hydrofluoric acid solution for 30 seconds and rinsed in deionized water prior to film deposition.

4.1.2 Sample set

Six wafers were prepared for deposition. Each of the samples was split into two halves, where one half was used for lifetime measurements, and the other half processed further into a suitable sample for C–V measurements. The lifetime samples received equal deposited films on both sides, while the C–V sample was deposited on the front side only.

Table 4-2 summarizes the design of the sample set. The set consist of four silicon nitride samples (SiN_x) and two stacks consisting of a silicon oxynitride (SiO_xN_y) capped by SiN_x. The buffer layer of the stacks are equal, while the capping layer is divided in two different compositions; one silicon rich and one nitride rich, with equal thicknesses. Two different SiN_x compositions were used for the nitride samples, one nitride rich film and one silicon rich film. The compositions were deposited with two thicknesses, 80 nm and 100 nm.

Sample	**1**	**2**	**3**	**4**	**5**		**6**	
Layer					Capping	Buffer	Capping	Buffer
Film type	SiN_x	SiN_x	SiN_x	SiN_x	SiN_x	SiO_xN_y	SiN_x	SiO_xN_y
SiH_4 flow (sccm)	10	5	10	5	20	45	10	45
Deposition time	7 min	7 min	5 min 15 s	5 min 15 s	5 min 15 s	9 s	5 min 15 s	9s
Nominal thickness (nm)	100	100	80	80	80	9	80	9

Table 4-2: Design of the sample set.

As mentioned in section 2.5.2, the nitride content will alter the electronic and optical properties of the film. A decreasing silane (SiH_4) flow will decrease the silicon content in the film, e.g. increase the x in SiN_x. This sample set was designed to allow testing of the passivation properties and their dependence of both composition and thickness.

4.1.3 Plasma-Enhanced Chemical Vapor Deposition (PECVD)

The samples were deposited using plasma-enhanced chemical vapor deposition, a process used for depositing thin films. An electric field is created in the chamber which ionizes the precursor gases to react over the substrate. The plasma allows the reaction rate of the precursors to be high, while keeping the processing temperature low. Figure 4-1 shows the PECVD reactor.

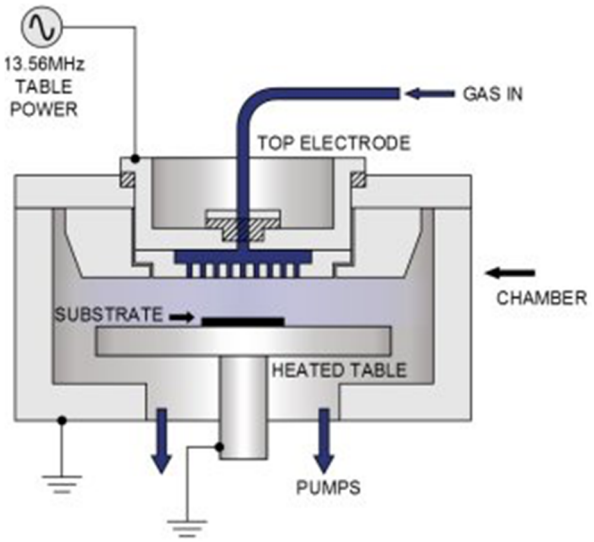

Figure 4-1: The PECVD reactor. Figure from (Oxford Instruments 2017).

The PECVD reactor used for this study was a PlasmaLab 133 system from Oxford Instruments. Table 4-3 shows the deposition parameters for the films. In total, there were three different nitride films and one oxynitride. The same oxynitride film was used as buffer layer for both the stacks.

Parameters	**Unit**	**a-SiN$_x$:H**	**a-SiN$_x$:H**	**a-SiN$_x$:H**	**SiO$_x$N$_y$**
Temperature	℃	400	400	400	130
RF power	W	40	40	40	50
Chamber pressure	mTorr	800	800	800	500
Silane flow	sccm	5	10	20	45
Ammonia flow	sccm	20	20	20	
Nitrogen flow	sccm	980	980	980	
Nitrous oxide	sccm				20

Table 4-3: Deposition parameters for the passivation films.

4.1.4 Metallization

The metallization was performed using a Kurt J. Lesker Company NANO 36 evaporation system. The samples are mounted on a stage vertically over a crucible containing an aluminum pellet. The chamber is pumped down to attain vacuum prior to metallization. A large current is used to heat the crucible so that the aluminum evaporates and a thin aluminum layer is deposited on the surfaces in the vacuum chamber, including the sample. The thickness of the aluminum layer is determined by the size of the aluminum pellet.

The C–V samples were turned into MIS-structures by covering the backside of the sample with aluminum. Further, a shadow mask was used to create electrodes on the front side of the samples. Figure 4-3 shows the front side of a metallized C–V sample. The shadow mask was created of a Si-wafer, using a laser to create a pattern of circular holes with diameters of 2 mm, 1.5 mm and 1 mm. The shadow mask covered the sample such that aluminum was deposited through the masks and onto the substrate. The backside of the MIS-structure was covered with 135 nm aluminum, while the thickness of the front electrodes was approximately 50 nm.

The lifetime samples needed metal contacts on both the front and backside for the PL-V measurements. A shadow mask formed the front side aluminum pads, with a thickness varying from 55 nm to 80 nm. Figure 4-2 shows the front side of a metallized PL-V sample. The backside contacts were created with silver paste. A small amount of silver paste was added to the corners of the backside and further scratched by a crystal pen to penetrate the dielectric film to obtain contact between the silver and the silicon substrate.

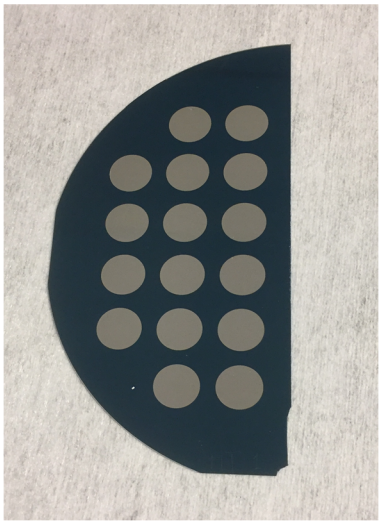

Figure 4-2: A metallized lifetime sample.

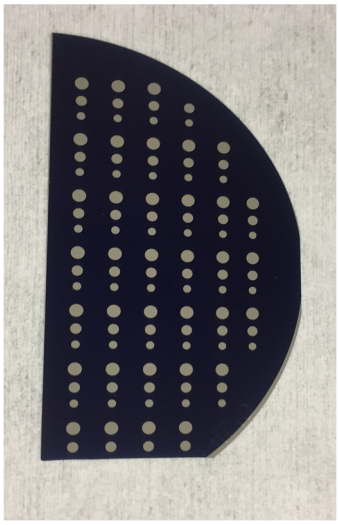

Figure 4-3:A C–V sample with electrodes

4.1.5 Annealing

The annealing process is conducted to improve the quality of the dielectric films and the contacts between the aluminum electrode and the silicon for the C–V samples. This high temperature process usually improves the minority carrier lifetime drastically; see e.g. Cheng et al. (2016).

A high temperature furnace with a heating zone of 80 cm and a belt speed of 8 cm/min was used to obtain a heating temperature of 400 ℃ for 10 minutes. The annealing process was supposed to be performed at 450℃, but the furnace was only able to reach 400 ℃ due to instrumental problems. The heat treatment may cause the metal electrodes to melt through the deposited film and damage the sample. The annealing was thus performed prior to metallization for all samples, except for the backside of the C–V samples. The aluminum–silicon transition is improved during annealing as a eutectic phase is formed at the interface.

4.2 Characterization

4.2.1 Ellipsometry

The ellipsometry, which was used to determine the refractive index and the thickness of the dielectric films, was performed on a setup from J. A. Woolam Co., Inc. Figure 4-4 shows an image of the setup.

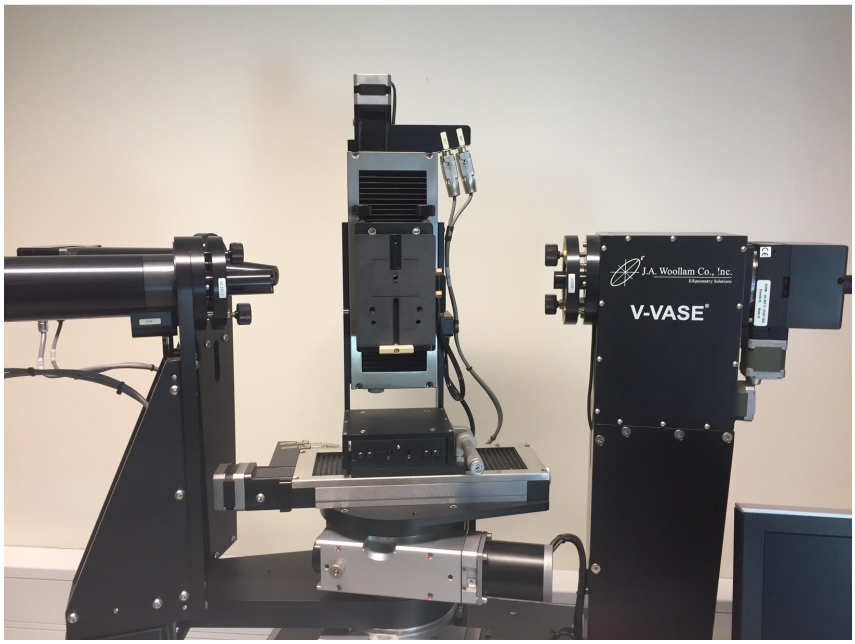

Figure 4-4: The ellipsometry setup.

4.2.2 Quasi Steady-State Photoconductance

The QSSPC measurements were performed on Sinton WCT-120TS setup. The experiments were carried out by using a generalized mode and changing the time constant from the longest setting (1/1) for the steady state measurements to the shortest setting (1/64) for transient measurements. Each of the measurement modes includes uncertainties regarding the simplifications in equation (3.6) and (3.7). To reduce the uncertainties, each sample was measured in both steady state and transient mode. The results of each measurement were shown in a Sinton-spreadsheet which was used to evaluate the data and to ensure satisfying results.

4.2.3 Photoluminescence Imaging

The PL-images were collected using a BT imaging LIS-R1 setup with and integrated QSSPC stage. As the QSSPC setup in the PL-I setup is known to produce fallacious data gained from the Sinton QSSPC measurements used to calibrate the images. The images were attained as counts per second and further calibrated with the data from the QSSPC measurement using MATLAB.

4.2.4 Capacitance-Voltage setup

The C–V characterization was performed using a Keithley 4200-SCS semiconductor system with a Signatone S-1060 QuieTemp Hot Chuck sample stage. Figure 4-5 shows the setup.

All work was performed using the CVU voltage sweep mode. The start voltage was set to 0 V with steps of –0.1 V and a sweep delay of 0.1 s. The AC-signal was 30 mV RMS and the frequency set to 100 kHz, which provided good results for all the samples. The hold time for the soaking voltage was set to 70 s, to ensure saturation of the electrode. The setup provides DC voltages of $\pm$30 V.

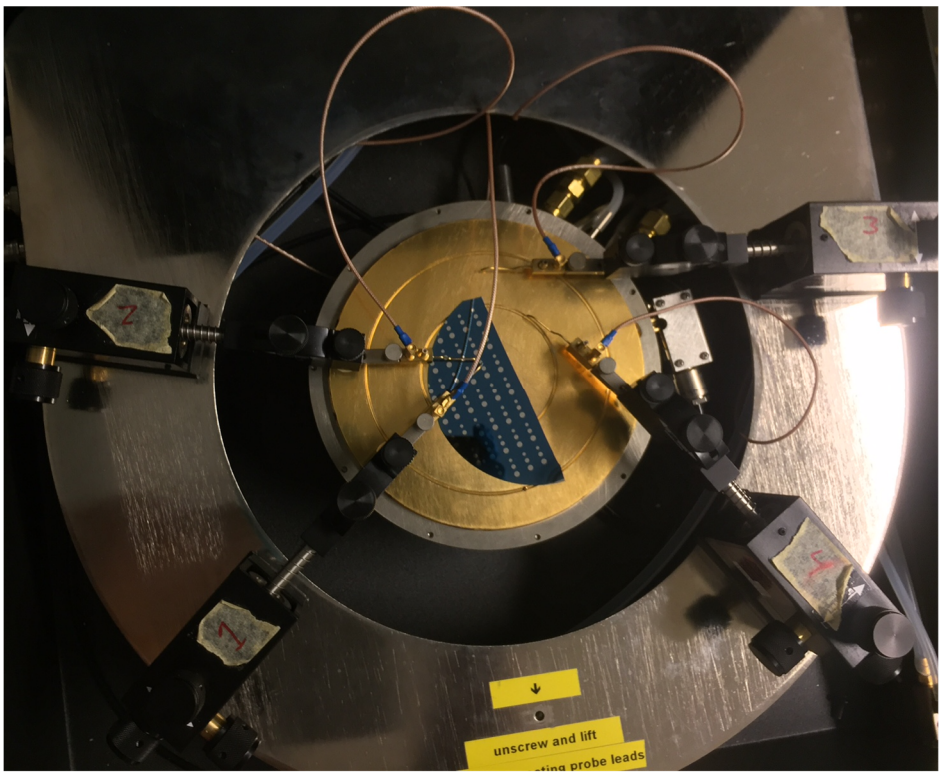

Figure 4-5: The C–V setup with a sample mounted on the stage.

4.2.5 Photoluminescence Under Applied Bias Setup

The PL-V measurements were performed on the same setup as the PL-I, but now using an integrated voltage setup. The bias was applied over the front side of the sample, while an ammeter was connected in series with the backside of the sample to monitor possible leakage currents. Figure 4-6 shows the PL-V setup.

To minimize errors from charging, the measurements were conducted by altering the applied voltage from positive to negative. The measurements were performed within setup's voltage limit of ± 10 V, with steps of 0.2 V. At integer measurement was a 0 V measurement performed, which was used to analyze the influence of charging. Several measurements were performed on each electrode to analyze the repeatability of the measurements.

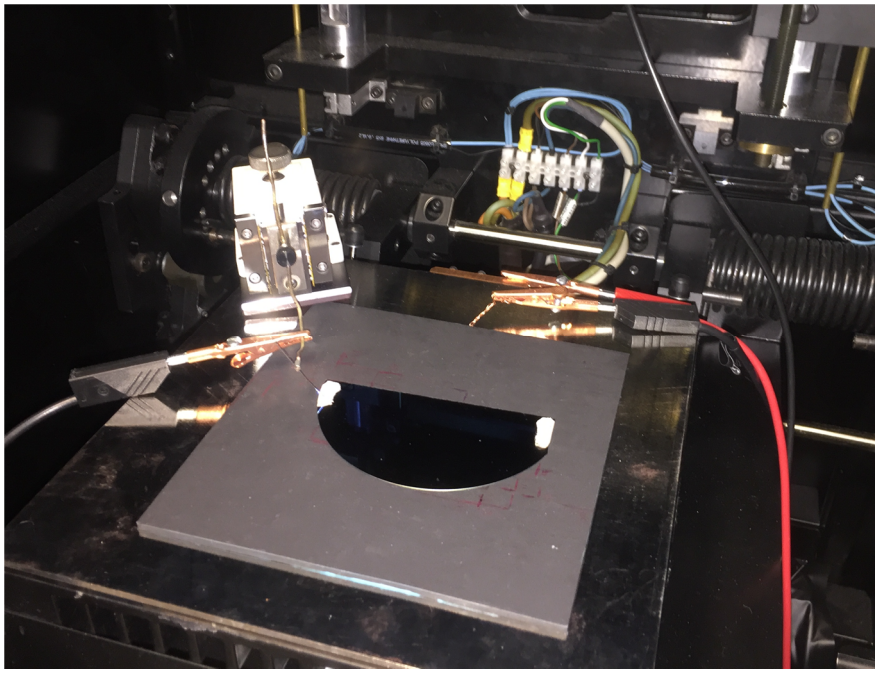

Figure 4-6: The PL-V setup with a sample mounted on the stage.

CHAPTER 5

RESULTS AND DISCUSSION

5.1 Optical properties

Knowledge of the optical properties is required for the lifetime measurement, which are based on optical excitation of the excess charge carriers. The thickness and the refractive index of the deposited thin films were measured using variable angle spectroscopic ellipsometry. Table 1 summarizes the results. In accordance with the theory, the thin films deposited using a higher SiH_4 concentration yield a higher refractive index. The reflection is found using a reflection calculator available online and is based on the refractive index and thickness of the film (PVeducation 2017). The results show that, among the samples with equal nominal thickness, the silicon rich samples yield higher reflection compared to the nitride rich samples at the excitation wavelength 630 nm.

The deposition parameters affect the thickness of the films, which is also shown in the results. The samples with the lowest silane flow are 5 nm thinner for the nitrides and 3 nm thinner for the oxynitirides. However, the thicknesses correspond well with the nominal thicknesses given in Table 4-2.

Sample	Film thickness (nm)	Refractive index (λ=630nm)	Reflection (λ=630nm)
1	110	1.88	14%
2	105	1.85	8%
3	85	1.88	1%
4	80	1.84	0
5	93	2.02	8%
6	90	1.87	2%

Table 5-1: Thickness and refractive index measured by ellipsometry.

The model used for fitting the experimental results is based on a single-layer model, which is valid for the nitride films. Due to the thin layer of oxide relative to the capping layer of nitride, the model was assumed acceptable for the stacks. Measurements done by a co-worker at IFE on a batch containing stacks showed that the difference between the results from a double layer model compared to a single layer model was small.

5.2 Lifetime measurements

5.2.1 Quasi-Steady State Photoconductance (QSSPC)

QSSPC measurements were performed to obtain a minority carrier lifetime versus injection level curve, where the lifetime was extracted at injection level 1×10^{15} cm^{-3}. Table 5-2 summarizes the results. All the measurements were carried out in the transient mode. Steady state measurements were carried out using the longest time constant (1/1), and transient measurements were carried out using the shortest time constant (1/64).

The measured τ_{eff} shows that the passivation is good, but hard to evaluate further without a lifetime reference. The measured effective lifetime of the nitrides is in the range of 72 – 134 µs, while the measured τ_{eff} for the stacks are in the range of 1419 – 1773 µs. The nitrides are performing as expected, but not extraordinarily, while the stacks yield a promising high τ_{eff}. A sample with better passivating properties, such as an a-Si:H film for passivation, could have been used as a lifetime reference and to estimate a lower limit for the bulk lifetime.

Sample	Steady state (µs)	Transient (µs)
1	112	-
2	79	80
3	129	138
4	68	75
5	-	1773
6	1433	1405

Table 5-2: Effective carrier lifetimes at $\Delta n = 1\times10^{15}$ cm^{-3}, measured by QSSPC.

The measurements were evaluated using the Sinton spreadsheet. The nitrides had the lowest measured lifetime in the batch, but, with the exception of sample one, had sufficiently high τ_{eff} to provide adequate results in both transient and steady state mode. The stacks have a noticeable higher effective lifetime, such that the steady state measurement was inadequate for sample 5.

Figure 5-1 shows the results of both steady state and transient measurements of sample 6. The left-hand plot in the figure shows the steady state measurement, while the transient measurement is shown to the right. At the injection level where the lifetime data is extracted, $\Delta n = 1.0{\times}10^{15}$ cm^{-3}, Sample 6 is just within the region of the steady state measurement. For a sample of longer lifetime, such as sample 5, this injection level will be out of range and the measurement unsuccessful.

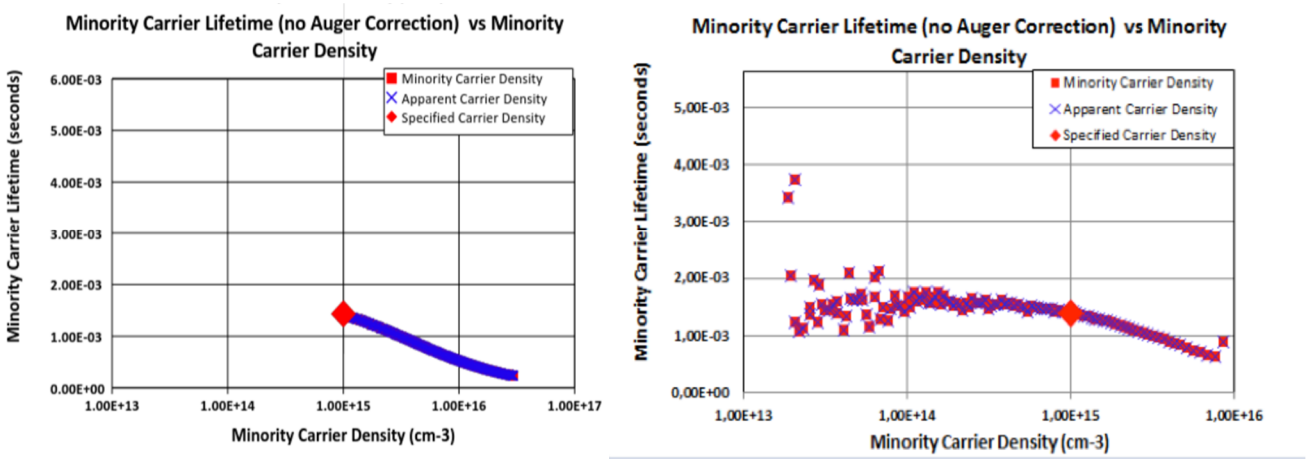

Figure 5-1: Effective lifetime versus injection level curves for sample 5. The left figure shows the results of the steady state measurement, while the figure to the right shows the transient QSSPC measurement.

5.2.1.1 SRV CALCULATIONS

Calculation of the surface velocity in equation (2.20) requires knowledge of the bulk lifetime, which is unknown for the samples used in this study. The highest lifetime measured in the QSSPC is 1773 µs, which is the lower limit of the bulk lifetime. In this case, the SRV would be zero for sample 5, and recombination would only occur in the bulk of the sample. By using equation (2.21), S_{max} is estimated by assuming an infinite bulk lifetime.

A calculation assuming different values of τ_b was performed in order to determine the range of possible SRV values yielded by each surface passivating material system. Figure 5-2 shows the results. The starting point of the calculations was $\tau_b = 1773$ µs and proceeded towards $\tau_b = 40\,000$ µs. At $\tau_b = 40\,000$ the difference between S_{max} and the calculated SRV was less than 0.4 cm/s. The average SRV increase from $\tau_b = 1773$ µs to $\tau_b = 40\,000$ µs is 8.2 cm/s.

The SRV for the silicon rich nitrides are in the range of 104 cm/s to 129 cm/s, while the nitride rich samples are in the range of 175 cm/s to 213 cm/s. The SRV of the stacks are in the range of 0.9 cm/s to 10 cm/s. These ranges are based on the assumption that an SRV of 0 cm/s is unlikely, such that the lowest limit is based on $\tau_b = 2000$ µs.

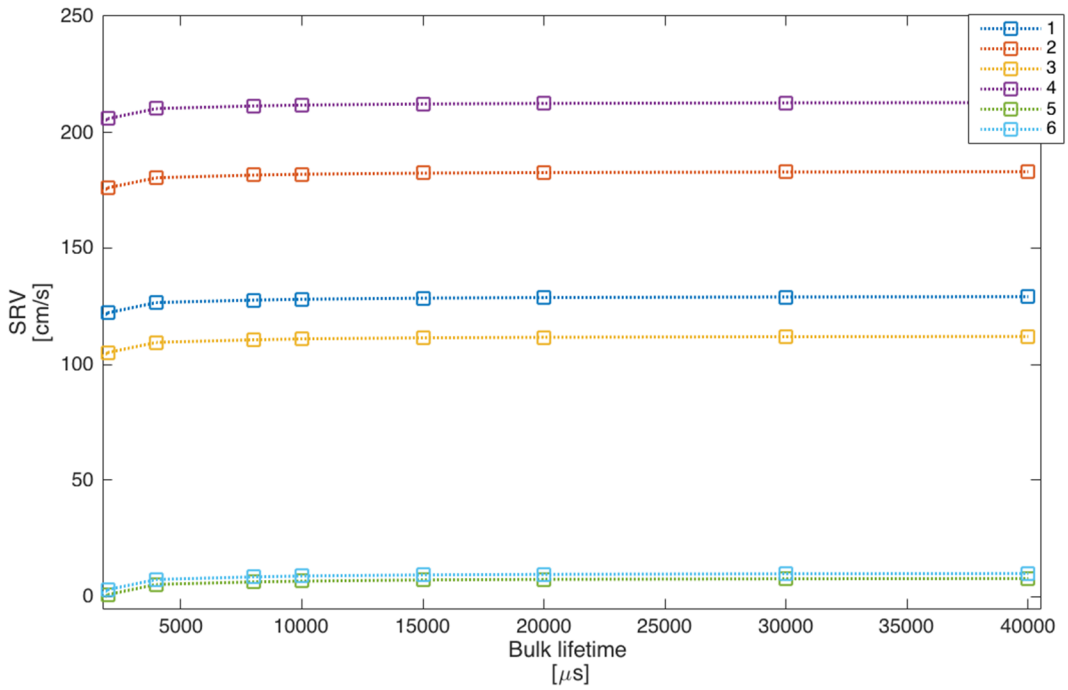

Figure 5-2: SRV of the six samples as a function of bulk lifetime.

5.2.2 Photoluminescence Imaging (PL-I)

The images shown in Figure 5-3 are obtained from the PL-I, and show the spatial quality of the samples. The images are not calibrated, and the colors are therefore not directly comparable. The bright yellow corresponds to a high lifetime, while blue is the lowest lifetime. All the samples suffer from poor quality towards the edges. The lines visible on sample 1 and 3 and on the left edge of sample 4 may be a result of scratches or tension weaknesses in the sample processing where the samples were divided in two. Small spots are detected on all the samples, which may be a result of impurities and dust. Visual inspections of the maps show that the edges should be avoided if possible during measurements. The upper part of sample 3 suffers from a lot defects, and measurement areas for this sample should therefore be chosen carefully.

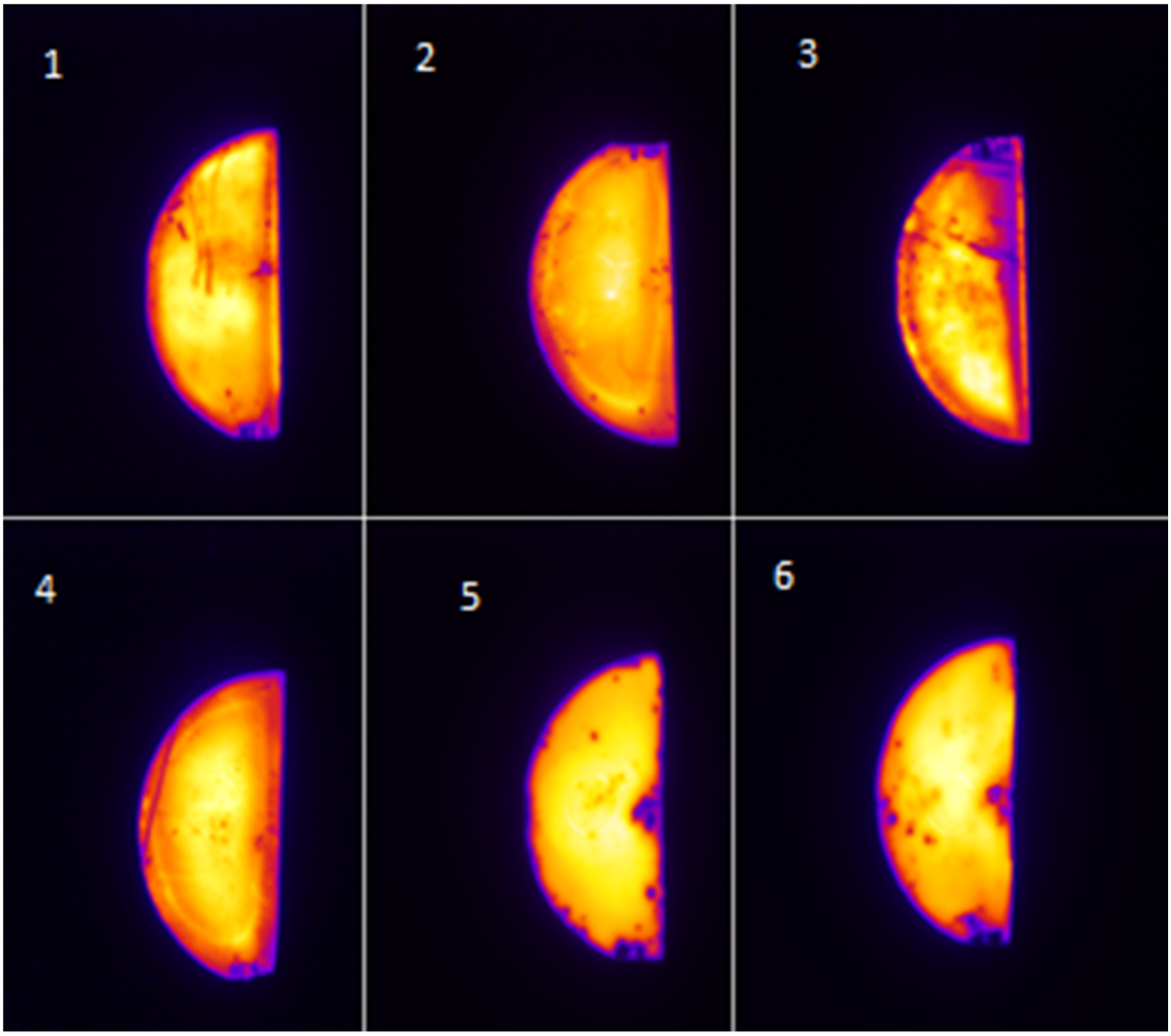

Figure 5-3: Spatial resolution of the six samples measured by PL-I.

5.2.3 Summary lifetime measurements

The lifetime measurements obtained from the QSSPC measurement show a difference between the compositions of the films. The nitride rich films obtained the lowest effective lifetime among the SiN_x samples, slightly below 100 µs, while τ_{eff} for the silicon rich nitrides exceeded 100 µs. The lifetime of the stacks was significantly larger than τ_{eff} for the nitrides, with measured values around 1500 µs. Comparing the two stacks shows that τ_{eff} for the silicon rich stack was higher than for the nitride rich stack. Subsequently to a higher effective lifetime is a smaller SRV calculated. Without knowing the bulk lifetime was the SRV calculated for different values of τ_b to get an idea of the range of the possible SRV. The calculation shows a stable SRV for τ_b values larger than 10 000 µs, as a result of the $1/\tau_b$ term in equation (2.20).

A level of measurement uncertainty must be considered both for the measurement procedure and for the QSSPC setup. The effective lifetime obtained from the QSSPC is limited to the area of the inductively coupled coil. Mapping of the samples obtained by PL-I shows some defects in the center of the samples which may have affected the QSSPC measurements. The maps of sample 1 and 3 displays scratches in the center of the samples. These areas have probably affected the QSSPC measurements, such that the measured lifetime might be lower than what a damage free sample would have returned. However, the QSSPC shows a realistic pattern; the silicon rich samples are expected to provide better chemical passivation, which is consistent with the results obtained.

5.3 Charge injection analysis

5.3.1 Capacitance – Voltage (C–V)

The initial CV-sweep was conducted without a pre-soaking voltage to determine V_{fb}, and subsequently the fixed charges of the dielectric films. The electrodes were then pre-soaked with a bias followed up by a new sweep to study the change in Q_f as a function of charging.

The C–V setup provides a pre-soak voltage up to $\pm$ 30 V. The voltage sweeps were performed using negative biases only to avoid hysteresis effects caused by charged K-centers. The pre-soak time was set to 70 s to ensure saturation (Bazilchuck et al. 2015). The soaking started at –10 V up to –30 V with –5 V steps. The sweeps were performed immediately after the charging to avoid discharging of the electrode, such that the measured Q_f corresponded to the soaking bias.

A typical C–V sweep for the nitride films is shown in Figure 5-4. the general results for nitride films were small hysteresis' and a steady increase in the flatband voltage with increasing soak voltage. The

initial V_{fb} for the nitrides were in the range –2.9 V to –4.1 V. At the highest soak voltage of –30 V, V_{fb} was in the range –9.5 V to –15.1 V.

A sweep of the 90 nm SiO_xN_y is shown in Figure 5-5, and the result is representative for the 93 nm SiO_xN_y in means of hysteresis. The general trend in the C–V results of the stacks is more hysteresis effects and a less consistent increase in the flatband voltage compared to the nitrides. V_{fb} of the 90 nm stack increased from –6.1 V to –12.5 V at –30 V soaking bias, and from -3.7 V to –9.6 V for the 93 nm stack.

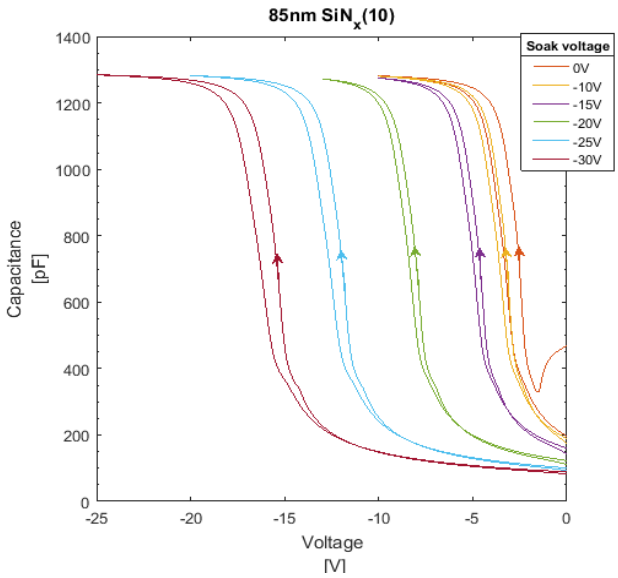

Figure 5-4: Typical C–V sweep of nitrides with soaking bias from -10V to -30V.

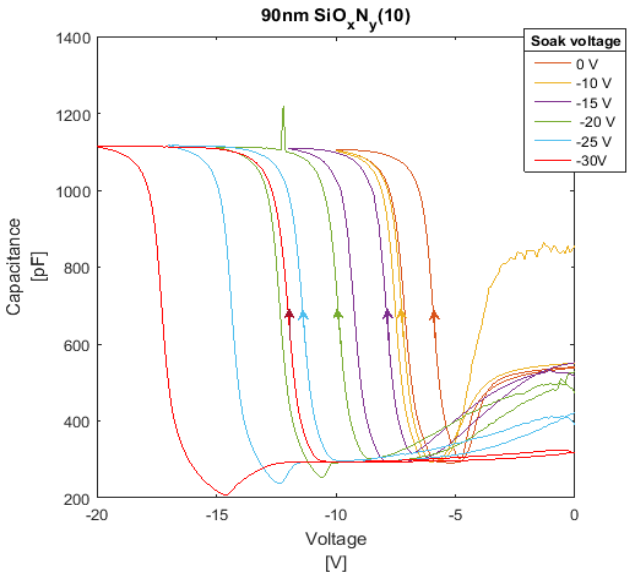

Figure 5-5 Typical C–V sweep of the oxynitrides with soaking bias from -10 V to -30 V.

The C–V sweeps were performed on several electrodes on each sample. Some of the electrodes were defect and provided fallacious data, such as negative capacitance and messy curves. The experiments conducted on the stacks were especially troublesome, due to the large amount of hysteresis and sensitivity for bias exposure. The samples had been presented to voltages up to –10 V for 0.1 s during the initial sweep, which did not interfere with the following measurements for the nitrides. The stacks however, were affected, such that it was necessary to use a new electrode on some of the following sweeps. This resulted in fewer complete sets with soaking voltage up to –30 V, due to a limiting number of electrodes. Whereas three to four of the nitrides were used for further analysis, only two to three sets of the oxynitrides were used.

5.3.1.1 FIXED CHARGE ANALYSIS

The Q_f analysis was performed on all the complete sets that provided adequate C–V data. Figure 5-6 and Figure 5-7 show the average Q_f value at each soaking biased for the nitrides and the stacks respectively.

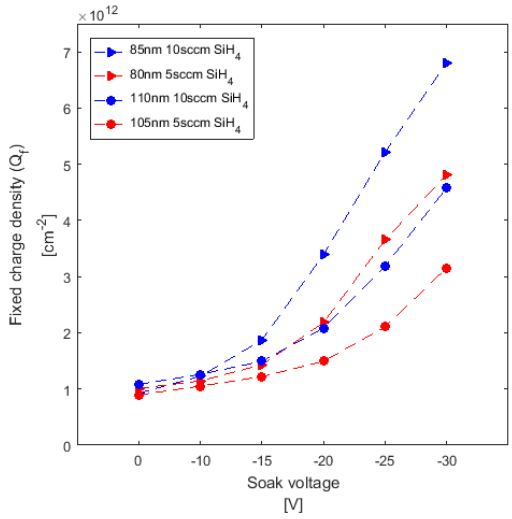

Figure 5-6: Fixed charge as a function of soak voltage for the nitrides.

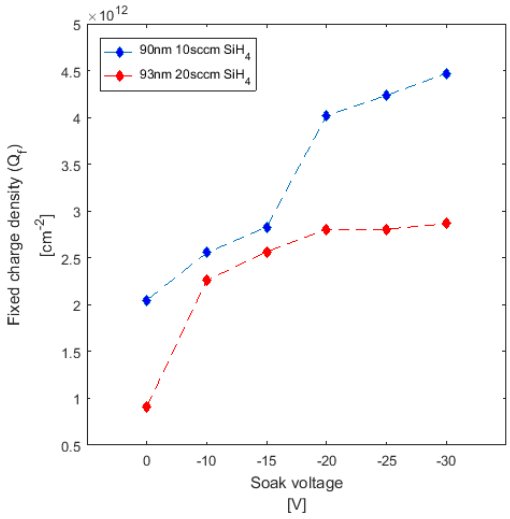

Figure 5-7 Fixed charge as a function of soak voltage for the stacks.

A visual inspection of the results shows that the films are chargeable. Q_f is increased from 1.0×10^{12} cm^{-2} to 6.8×10^{12} cm^{-2} for the nitrides and from 9.1×10^{11} cm^{-2} to 4.5×10^{12} cm^{-2} for the oxynitrides. Q_f of the nitrides are all increasing steadily, while each of the oxynitride samples have one abrupt increase before flattening. Comparing the maximum fixed charge density of the nitrides and the stacks shows that the best performing sample of the nitrides has twice as high Q_f than the best performing oxynitride. The sample with the lowest Q_f in the batch is the silicon rich oxynitride. Another important mechanism is that the nitrides show no sign of charge saturation towards –30 V soaking bias, while the stacks are flattening towards the higher biases. This indicates that the nitrides in this batch are more chargeable than the stacks.

5.3.1.2 NITRIDES

In Figure 5-6, data points with the same shape (triangular or circular) have equal nominal thicknesses, while the red and the blue color separate the two different nitride compositions.

A general trend of almost no increase in Q_f until the soaking voltage exceeds –10 V is observed. Q_f is still increasing for all the nitrides at -30 V, which shows that it might be possible to inject more charge into the films.

A slightly steeper slope can be observed for the silicon rich samples, and the 85 nm thick sample reach the highest fixed charge of 6.8×10^{12} cm^{-2}. The nitride rich 80 nm sample yields the second highest fixed charge of 4.8×10^{12} cm^{-2}. These results are expected due to the capacitance of the insulating layer which depends on the thickness of the film, as more charge is expected to be stored in a thinner film.

The nitride rich films were expected to contain a larger concentration of fixed charges, and thus provide more field effect passivation. This effect is not observed in these measurements. Charging of the films shows that the response with regards to increase in Q_f is more effective for the thinner films among the samples with equal compositions.

5.3.1.3 STACKS

The red line in Figure 5-6 corresponds to the silicon rich sample, and the blue corresponds to the nitride rich sample.

The initial Q_f of the nitride rich stack of 2.0×10^{12} cm^{-2} is the highest measured in batch, which is 1.1×10^{12} cm^{-2} higher than the average of the other samples.

The behavior of the stacks differs from the nitride behavior. Both samples have a similar abrupt rise in Q_f, but the effect occurs at different soak voltages. For the silicon rich sample, the increase in Q_f from 0 V to –10 V is 1.2×10^{12} cm^{-2}. The increase in the nitride rich sample from -15 V to -20 V is 1.3×10^{12} cm^{-2}.

Both samples show a tendency to flatten out after the abrupt increase. The highest Q_f at –30 V soaking voltage of the stacks is almost half of what is measured in the nitrides.

The film thickness of these samples only differs by 3 nm, such that the capacitance will be nearly equal. The difference of Q_f in the samples is therefore assumed to be due to composition, where the nitride rich capping layer provide greater field effect passivation compared to the silicone rich capping layer.

5.3.1.4 FILM CAPACITANCE

The capacitance used for the Q_f analysis is based on the measured C_i in the CV sweeps. C_i was calculated using equation (3.16) and is summarized together with the measured capacitance in Table 5-3.

		Insulator capacitance		
Sample	**Composition**	**Measured (pF)**	**Calculated (pF)**	**Deviation (%)**
1	SiN_x	943	1066	11,5
2	SiN_x	1041	1118	6,9
3	SiN_x	1281	1381	7,2
4	SiN_x	1381	1467	5,9
5	SiO_xN_y	892	1262	29,3
6	SiO_xN_y	1113	1304	14,7

Table 5-3: The calculated and measured capacitance for the insulator. The deviation between the results are listed in the last column.

The results in Table 5-3 show that the measured values are closely linked to, but consistently smaller than the calculated values.

The measured value is 6% to 15% lower than the calculated capacitance. The area of the pads used for the calculations are based on the diameter of the shadow mask and thus give rise to an uncertainty in the calculations. The actual area could be measured using a microscope, but this was unfeasible due to the limited time available. C_i of the stacks are estimated assuming that the oxide layer (~6 nm) is negligible relative to the thickness of the nitrides (~90nm), which may be the reason for the deviation. The calculation is further based on the assumption that the relative permittivity of the nitride layer is 7.5, which is based on an average from available literature, which vary from 7–8. The thickness used for calculating the capacitance is obtained from the ellipsometry, which, as mentioned, was obtained using a single level model for all the samples, including the stacks.

5.3.2 Photoluminescence imaging under applied bias (PL-V)

The PL-V measurements were conducted in the range of 0 V to ±10 V, which is the available range of the setup. The experiments were performed with steps of 0.2 V and alternating bias to minimize the influence of charging. A 0 V measurement was performed at each integer to monitor the charging effect. The experiments resulted in intensity versus voltage curves which were calibrated with PL images and QSSPC measurements. τ_{eff} versus voltage curves were produced and the Girisch model was used for simulation.

5.3.2.1 NITRIDES

Figure 5-8 shows the PL-V results of the nitrides. The experimental data is shown as squares, while the simulation curve is presented as a line. Table 5-4 summarizes the fitted parameters.

Figure 5-8 shows that the flattening of sample 1 and 3, the silicon rich samples, are outside the measurement range. Due to the positive charges in the films is the smallest τ_{eff} found at negative bias. The limited range of ±10 V for samples of positive fixed charge will thus provide more information in inversion.

The minimum point *of* τ_{eff} is in the range –2.4 V and –3.4 V, which is smaller, but close to V_{fb} found in the C–V measurements. Samples 1 and 3 have a steeper slope around the minimum τ_{eff}. These are the samples of higher silicon concentration and are thus expected to have a higher degree of chemical passivation.

The right slope of the minimum τ_{eff} is found to be steeper than the left slope in all measurements. Table 5-4 shows that $S_{p0} > S_{n0}$ for all samples, which explains the asymmetry in the measurements. This implies a higher recombination activity for the electrons in inversion.

The capture cross ratio is found to be bigger than 1 for all samples. Comparing the samples of nominal equal thickness show that σ_n/σ_p for the nitride rich samples are smaller compared to the silicon rich samples. However, the smallest capture cross section is found for samples 1 and 2 - the 100 nm thick samples - with σ_n/σ_p of 1.97 and 1.30 respectively.

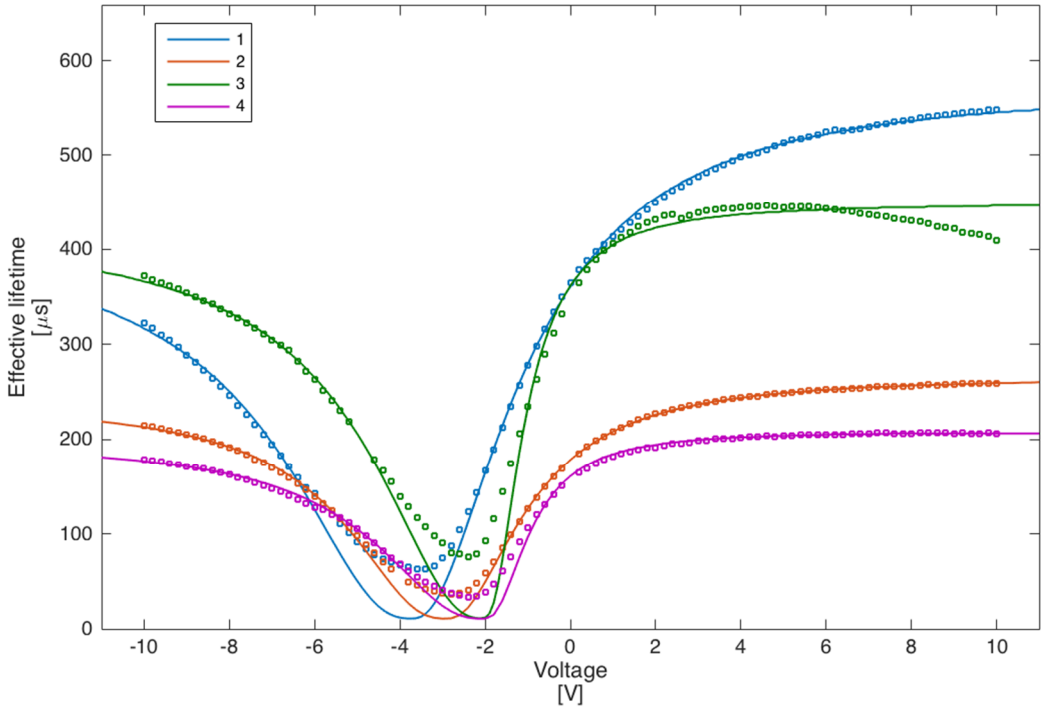

Figure 5-8: Effective lifetime as a function of gate voltage, measured by PL-V.

		Sample			
Parameter	**Unit**	**1**	**2**	**3**	**4**
Q_f	(cm^{-2})	1.1×10^{12}	1.2×10^{12}	6.3×10^{11}	6.7×10^{11}
S_{n0}	(cm/s)	5.26×10^{4}	4.27×10^{4}	6.47×10^{4}	1.53×10^{5}
S_{p0}	(cm/s)	2.67×10^{4}	3.29×10^{4}	6.91×10^{3}	2.34×10^{4}
$S_{min,n}$	(cm/s)	26.3	28.2	25.5	105.1
$S_{min,p}$	(cm/s)	6.7	8.3	20.4	96.9
σ_n/σ_p		1.97	1.30	9.36	6.53

Table 5-4: PL-V simulations of the nitrides.

It should be noted that the minimum τ_{eff} is lower for the simulated curve than the experimental data. This causes a shift in V_{fb} and Q_f from what obtained in the C–V measurements. This is a result of the weakness of the Girisch model at high SRVs.

Table 5-5 summarizes the SRVs for the nitrides at flatband. The results show that the surface recombination velocity at $\psi_s = 0$ is highest for the nitride rich samples. This corresponds well with the theory, as increasing silicon content in the film improves the chemical passivation of the film.

Sample	SRV (Vfb)
1	472
2	962
3	378
4	1102

Table 5-5: Experimental values of SRV obtained by PL-V.

Figure 5-9 shows the SRV obtained from both QSSPC and PL-V. The plot shows that the SRV measured by QSSPC is larger than the PL-V measurement. The largest change is observed in the silicon rich samples. The major change is due to the annealing of the samples, which was performed after the QSSPC measurement. SVR obtained at 0 V for the silicon rich samples was 35 cm/s for the 100 nm sample and 39 cm/s for the 80 nm sample. In comparison, the SRV for the nitride rich films were 123 cm/s and 145 cm/s for the 100 nm and 80 nm films respectively. A significant difference from what observed in the QSSPC measurements which was performed prior to annealing.

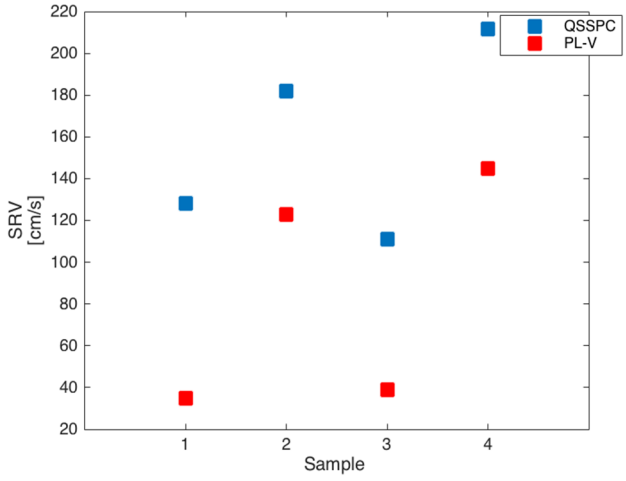

Figure 5-9: SRV measured by QSSPC and PL-V.

5.3.2.2 STACKS

NITRIDE RICH STACK

Figure 5-10 shows the measured lifetime and the leakage current of the nitride rich stack as a function of applied voltage. The lifetime plot has an unexpected shape, as τ_{eff} at V_{fb} is not the lowest lifetime measured. The leakage current is stable around 0 mA from –6 V to 2 V. The measured lifetime is dropping for voltages outside this range.

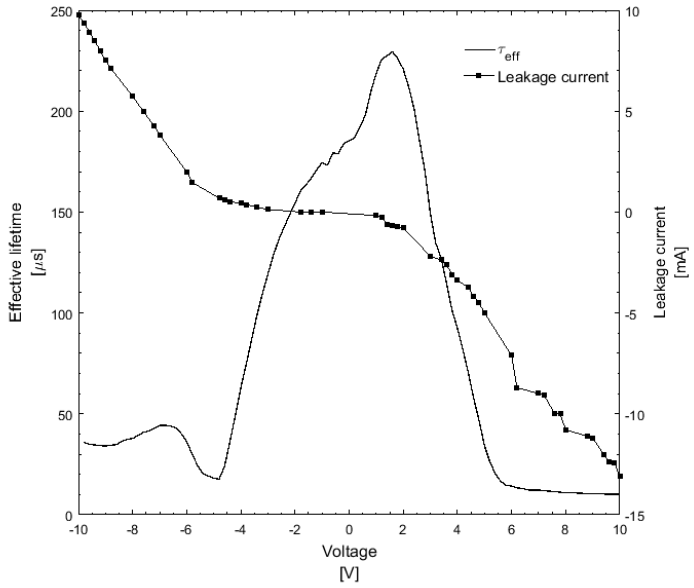

Figure 5-10: Effective lifetime and leakage current plotted as a function of voltage for the nitride rich stack.

The simulation was performed in the range from –6 V to 1 V to avoid effects of the leakage current. As $V_{fb}$is found at –5.2 V, the measurement provided little information towards accumulation. Q_f was found to be 4.2×10^{13} cm^{-2}. Compared to the Q_f found in the C–V measurements (2.1×10^{12} cm^{-2}) this seems unrealistic. The C–V measured V_{fb} at –6.1 V, while the PL–V measurement shows V_{fb} at –5.2 V. The shift in V_{fb} in the PL–V measurement suggests that the fixed charge density should be smaller, while the simulations show the opposite.

It is possible to measure the surface recombination parameter for holes from the minimum τ_{eff} to 1 V. This was found to be 2.4×10^{4} cm/s. While there is high uncertainty related to the measurement of this sample, S_{p0} for this sample is in the same range the nitride, shown in Table 5-1.

SILICON RICH STACK

Figure 5-11 shows the simulation and the measured τ_{eff} for the silicon rich stack and Figure 5-12 shows the SRV calculated from the measured τ_{eff}. The lifetime curve show steep slopes at both sides of V_{fb}, which indicates a high degree of chemical passivation. The highest effective lifetime, 5800 µs, is measured in inversion. The results yield an SRV less than 1 towards accumulation and inversion. This calculation is based on an infinite τ_b, the SRV shown in Figure 5-12 is thus the S_{max} described in equation (2.21).

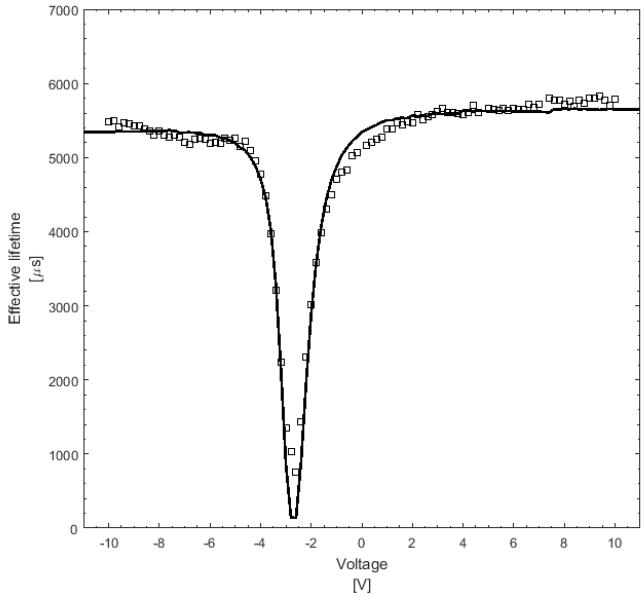

Figure 5-11: Effective lifetime as a function of applied voltage for the silicon rich stack.

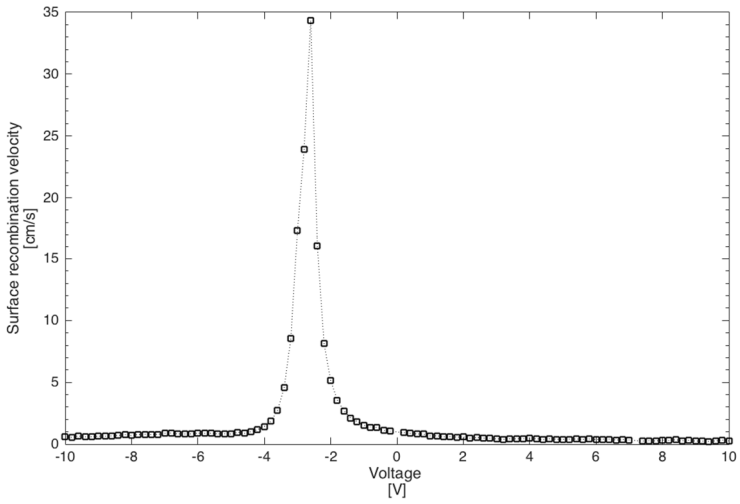

Figure 5-12:Surface recombination velocity calculated from the measured τ_{eff}.

Table 5-6 shows the simulated parameters for silicon rich stack. The results show the smallest values of the surface recombination parameters and the smallest $S_{min,n}$ and $S_{min,p}$ in the sample set. The capture cross ratio is less than 1. The capture cross ratio suggests that the recombination activity is higher towards inversion.

V_{fb} is found at –2.6 V in the PL–V, which is lower to V_{fb} measured in C–V (–3.7 V). However, the Q_f measurement matches well, as the C–V measurement yields 9.1×10^{11} cm^{-2}. A lower PL–V value of V_{fb} is consistent with a lower Q_f, and the difference between the C–V measurements and the PL–V is thus expected to be due to the Girisch models poor ability to provide full information at low SRVs.

Parameter	**Unit**	
$\boldsymbol{Q_f}$	(cm^{-2})	9.0×10^{11}
$\boldsymbol{S_{n0}}$	(cm/s)	87
$\boldsymbol{S_{p0}}$	(cm/s)	261
$\boldsymbol{S_{min,n}}$	(cm/s)	0.68
$\boldsymbol{S_{min,p}}$	(cm/s)	0.38
$\boldsymbol{\sigma_n/\sigma_p}$		0.33

Table 5-6: Simulated parameters for the silicon rich stack.

5.3.2.3 ZERO VOLT MEASUREMENTS

Zero volt measurements were performed at each integer during the PL-V measurements. Figure 5-13 shows a plot of the results. The plot of the nitride films and the nitride rich stack shows that the detected counts are stable during the measurements, which means that the altering bias is neutralizing the charge at each measurement. The silicon rich stack sample is stable between –3 V and 2 V. The charge effect is especially large for greater positive biases, while a small increase is seen for the increasing negative bias measurement. Still, the effect is not detectable in the simulation shown in Figure 5-11. However, this may have influenced the measurements shown in Figure 5-11 and Figure 5-12.

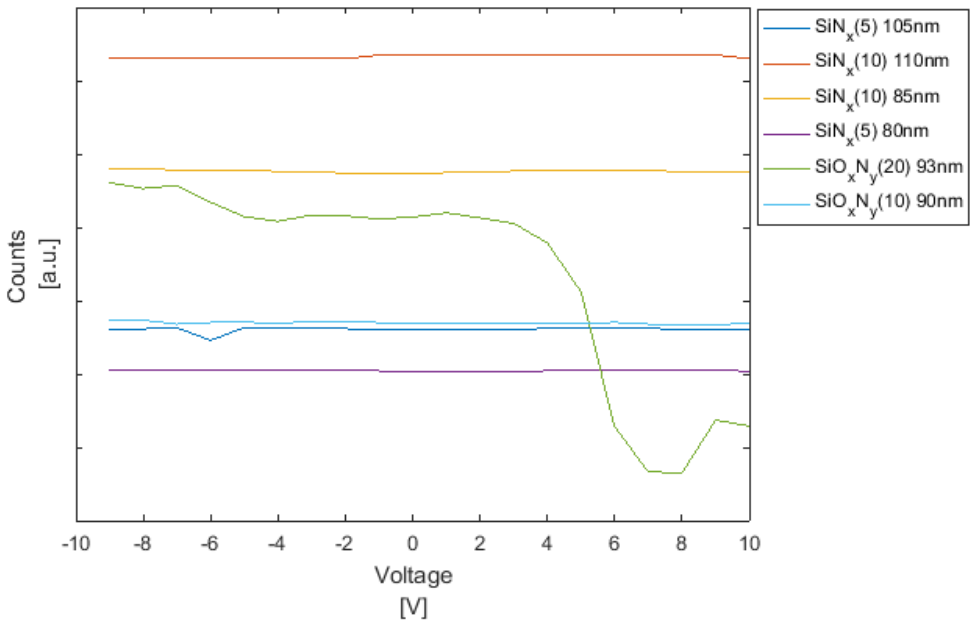

Figure 5-13: 0 V measurements.

5.3.3 Summary charge injection analysis

The C–V analysis shows that the fixed charge density has increased for all sample as a function of charging. The nitrides have shown to be more chargeable than the nitrides, with a steady increase for higher pre-soak voltages. The thinnest samples have the highest increase of the samples and the composition seems to be less influential.

The electric field created by pre-soak values of less than –10 V shows to be too small for the K-center transmission in the nitrides, such that no increase in Q_f is observed for the small pre-soak values. This is consistent with the findings of Bazilchuck et al. (2015). The composition seems to be more important among the stacks, both with regards to charging and the pre-charge experiments. The nitride rich sample had the highest initial fixed charge density, but the total increase was much lower than the Q_f increase of the nitrides.

The analysis regarding the nitrides are more complex. Higher hysteresis effects were observed and the increase in Q_f was less consistent. An increase of Q_f was observed for smaller pre-soak values below –10 V. This voltage was too small for the K-center to transmit to their positive states for the nitride samples, which shows an effect of the difference of the interfaces between the nitrides and the stacks.

The PL–V results show a difference between the composition among the nitrides. The silicon rich samples yield the highest effective lifetime. A difference of almost 350 µs was observed between the 100 nm silicon rich sample and the 80 nm nitride rich sample towards inversion. Both of the silicon rich samples yield a steep slope on both sides of the minimum τ_{eff}, which indicates a high degree of chemical passivation. This is also observed for the SRVs shown in Figure 5-9. When comparing the samples with equal thicknesses, the silicon rich sample has the lowest SRV. The PL–V measurement for the nitride rich stack was unsuccessful due to leakage currents. The silicon rich stack shows a good chemical passivation and a very high τ_{eff}. However, the zero volt measurements show that the measurement was effected by charging.

CHAPTER 6

CONCLUSION

This study has examined the properties of six different passivation layers, four nitrides and two stacks. The object of this work was to increase the understanding of the possibility of increasing the charge carrier density in silicon nitride films for improved field effect passivation. The properties that have been investigated are thickness, composition and the importance of field effect passivation relative to chemical passivation. Further is the suitability of the characterization methods is discussed and the passivation properties of the stacks is compared to the passivation properties of the single layer nitrides.

The effective lifetime measured by QSSPC showed that the stacks yields a higher effective lifetime relative to the nitrides and subsequently a lower SRV. τ_{eff} was observed to be higher for all the silicon rich samples compared to the nitride rich samples. The same pattern was observed among the nitrides for the PL–V measurements. The silicon rich samples yield the highest τ_{eff}, where the difference between the 100 nm samples was approximately 300 µs. SRV obtained at flatband conditions showed lower values for the silicon rich samples, implying a better chemical passivation for these samples.

With regards to charging in the C–V experiments, the stacks were less chargeable than the nitrides. An upper limit for charging of the nitrides was not reached, while the charge density for the stacks flattened out as the pre-soak voltages reached –20 V. The highest obtained Q_f for the stack is 4.5×10^{12} cm^{-2}, while the highest obtained Q_f for the nitrides is 6.8×10^{12} cm^{-2}.

The nitrides have proven to be chargeable. A steady increase of Q_f was observed, and the charge density was still increasing at the highest pre-soak voltage available. Measurements performed prior to soaking exhibited values of Q_f at approximately 1.0×10^{12} cm^{-2} for all nitrides. The thickness was shown to be the most influential parameter among the stacks with regards to charging. The thinnest samples reached the highest Q_f, with the silicon rich sample being the best performing of the 80 nm samples.

The composition showed a difference of the charging of the stacks, where the nitride rich stack was the best performing sample with both the highest initial and –30 V Q_f.

The characterization methods have attained as-expected results with regards to the theory for all nitrides. For the stacks, the electrical characterization methods, C–V and PL–V, have provided more complex results. The PL–V measurements was affected by leakage currents and charging affects observed at the 0 V measurements. Q_f as a function of charging in the C–V is less consistent, with abrupt increases and flattening of curves being observed.

However, the stacks have proven to provide better passivation. The lowest SRV has been obtained for the stacks. The τ_{eff} obtained at the PL–V measurement shows an effective lifetime of approximately 5800 µs, which is significantly higher than the best performing nitride at 550 µs.

CHAPTER 7

FURTHER WORK

Charging saturation: Due to instrument limitations was the highest pre-soak voltage –30 V. Q_f was still increasing for all nitrides at this point. Further charging could be performed using an external voltage source to investigate the upper limit for Q_f.

Effective lifetime for increased Q_f: The nitrides showed to be chargeable, and is thus expected to yield better field effect passivation. However, the effective lifetime as a function of increased fixed charge is not investigated.

Stack configuration: The results obtained from the electrical characterization methods have shown non-trivial behavior. Further research could be performed to investigate whether the effects shown is general for all stacks because of the stack configuration or a result of the composition of the materials.

Stack thickness: The stack samples used in this study was of equal nominal thickness. The thickness of the nitrides was observed to be the main property with regards to charging. Thinner stacks could be explored for a possibility of reaching a higher Q_f as a function of charging.

Bibliography

Aberle, A. G. (1999). *Advanced Surface Passivation and Analysis* Center for Photovoltaics Engineering, University of New South Wales

Aberle, A. G. (2000). Surface passivation of crystalline silicon solar cells: a review. *Progress in Photovoltaics: Research and Applications*, 8 (5): 473-487.

Aberle, A. G. (2001). Overview on SiN surface passivation of crystalline silicon solar cells. *Solar Energy Materials & Solar Cells*, 65.

Bazilchuck, M., Haug, H. & Marstein, E. S. (2015). Modulating the fixed charge density in silicon nitride films while monitoring the surface recombination velocity by photoluminescence imaging. *Applied Physics Letters*, 106.

Bazilchuck, M. S. (2014). *Improved Induced Diode Photodetectors by Increased Charge in PECVD Amorphous Silicon Nitride*: Norwegian University of Science and Technology, Nanotechnology.

Cheng, X., Haug, H., Sabatino, M. D., Zhu, J. & Marstein, E. S. (2016). Electronic Properties of a-SiOxNy :H/SiNx Stacks for Surface Passivation of P-Type Crystalline Si Wafers. *IEEE Journal of Photovoltaics*, 6 (5): 1103-1108.

Cuevas, A. & Macdonald, D. (2003). Measuring and interpreting the lifetime of silicon wafers. *Solar Energy Materials and Solar Cells*, 76.

Haug, H., Nordseth, Ø., Monakhov, E. V. & Marstein, E. S. (2012). Photoluminescence imaging under applied bias for characterization of Si surface passivation layers. *Solar Energy Materials and Solar Cells*, 106: 60-65.

Haug, H. (2014). *New methods for investigation of surface passivation layers for crystalline silicon solar cells*. Ph.D.: University of Oslo, Department of Physics. 106 pp.

Haug, H., Nordseth, Ø., Monakhov, E. & Marstein, E. S. (2014). Investigation of Carrier Recombination at the SiO2/c-Si Interface by Photoluminescence Imaging Under Applied Bias. *IEEE Journal of Photovoltaics*, 4 (1): 374-379.

Haug, H. (2017). *Effect of SRV* Personal communication.

Herlufsen, S., Schmidt, J., Hinken, D., Bothe, K. & Brendel, R. (2008). Photoconductance-calibrated photoluminescence lifetime imaging of crystalline silicon. *physica status solidi (RRL) – Rapid Research Letters*, 2 (6): 245-247.

IEA, International Energy Agency (2016). Medium-Term Market Report 2016, Market Analysis and Forecast to 2021.

ITRPV, Interntational Technology Roadmap for Photovoltaic. (2016). 2015 Results including maturity reports.

Mack, S., Wolf, A., Brosinsky, C., Scheimeisser, S., Kimmerle, A., ., Saint-Cast, P., Hofmann, M. & Biro, D. (2011). Silicon Surface Passivation by Thin Thermal Oxide/PECVD Layer Stack Systems. *IEEE Journal of Photovoltaics*, 1 (2): 10.

Nagel, H., Berge, C. & Aberle, A. G. (1999). Generalized analysis of quasi-steady-state and quasi-transient measurements of carrier lifetimes in semiconductors. *Journal of Applied Physics*, 86 (11): 6218-6221.

Oxford Instruments. (2017). *Plasma Enhanced Chamical Vapour Deposition (PECVD)*. Available at: https://www.oxford-instruments.com/products/etching-deposition-and-growth/plasma-etch-deposition/pecvd (accessed: 15.01).

PVeducation. (2017). *Anti-Reflection Coatings*. Available at: http://www.pveducation.org/pvcdrom/anti-reflection-coatings (accessed: 10.01).

REN 21. (2016). Renewables 2016 - Global status report.

Schmidt, J., Lauinger, T., Aberle, A. G. & Hezel, R. (1996, 13-17 May 1996). *Record low surface recombination velocities on low-resistivity silicon solar cell substrates*. Conference Record of the Twenty Fifth IEEE Photovoltaic Specialists Conference - 1996. 413-416 pp.

Schmidt, J., Kerr, M. & Cuevas, A. (2001). Surface passivation of silicon solar cells using plasma-enhanced chemical-vapour-deposited SiN films and thin thermal SiO 2 /plasma SiN stacks. *Semiconductor Science and Technology*, 16 (3): 164.

Schroder, D. K. (2006). *Semiconductor material and device characterization* vol. 3: John Wiley & Sons, Inc.

Sinton, R. A., Cuevas, A. & Stuckings, M. (1996). Quasi-steady-state photoconductance, a new for solar cell material and device characterization *25th IEEE Photovoltaic Specialists Conference* 4.

Sproul, A. B. (1994). Dimensionless solution of the equation describing the effect of surface recombination on carrier decay in semiconductors. *Journal of Applied Physics*, 76 (5): 2851-2854.

Trupke, T., Mitchell, B., Weber, J. W., McMillan, W., Bardos, R. A. & Kroeze, R. (2012). Photoluminescence Imaging for Photovoltaic Applications. *Energy Procedia*, 15: 135-146.

Norges miljø- og biovitenskapelig universitet
Noregs miljø- og biovitskapelege universitet
Norwegian University of Life Sciences

Postboks 5003
NO-1432 Ås
Norway